

1 **Tectonic interactions during rift linkage: Insights from analog and**  
2 **numerical experiments**

3  
4 *Timothy Chris Schmid<sup>1</sup>, Sascha Brune<sup>2,3</sup>, Anne Glerum<sup>2</sup>, and Guido Schreurs<sup>1</sup>*

5  
6 <sup>1</sup>*Institute of Geological Sciences, University of Bern*

7 <sup>2</sup>*Helmholtz Centre Potsdam – GFZ German Research Centre for Geosciences, Potsdam, Germany*

8 <sup>3</sup>*Institute of Geosciences, University of Potsdam, Potsdam, Germany*

Deleted: <sup>3</sup>University

Deleted: -Golm

9  
10 *Corresponding author Timothy Schmid: [timothy.schmid@geo.unibe.ch](mailto:timothy.schmid@geo.unibe.ch)*

11 *Institute of Geological Sciences, University of Bern, Baltzerstrasse 1+3, CH-3012 Bern, Switzerland*

12  
13 **Keywords:** *Numerical modelling, analog modelling, stress deflection, rift interaction, rift*  
14 *propagation*

15  
16 **Abstract**

17 Continental rifts evolve by linkage and interaction of adjacent individual segments. As rift  
18 segments propagate, they can cause notable re-orientation of the local stress field so that  
19 stress orientations deviate from the regional trend. In return, this stress re-orientation can  
20 feed back on progressive deformation and may ultimately deflect propagating rift segments  
21 in an unexpected way. Here, we employ numerical and analog experiments of continental  
22 rifting to investigate the interaction between stress re-orientation and segment linkage. Both  
23 model types employ crustal-scale two-layer setups where pre-existing linear heterogeneities  
24 are introduced by mechanical weak seeds. We test various seed configurations to investigate  
25 the effect of i) two competing rift segments that propagate unilaterally, ii) linkage of two  
26 opposingly propagating rift segments, and iii) the combination of these configurations on  
27 stress re-orientation and rift linkage. Both the analog and numerical models show counter-

30 intuitive rift deflection of two sub-parallel propagating rift segments competing for linkage  
31 with an opposingly propagating segment. The deflection pattern can be explained by means  
32 of stress analysis in numerical experiments where stress re-orientation occurs locally and  
33 propagates across the model domain as rift segments propagate. Major stress re-orientations  
34 may occur locally, which means that faults and rift segment trends do not necessarily align  
35 perpendicularly to far-field extension directions. Our results show that strain localization and  
36 stress re-orientation are closely linked, mutually influence each other and may be an important  
37 factor for rift deflection among competing rift segments as observed in nature.

38

## 39 **1. Introduction**

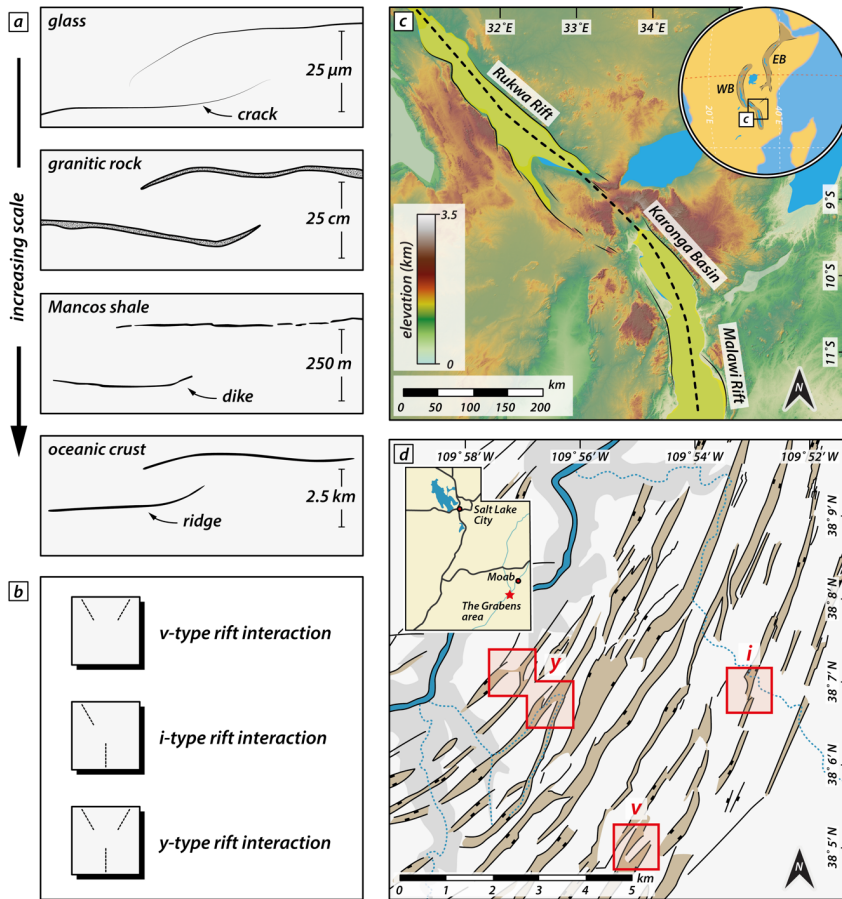
40 Continental rifting involves brittle faulting and the formation of subsiding rift basins. In places  
41 where individual rift segments are in proximity, they may interact and link when segments  
42 propagate and the rift system matures (Morley et al., 1990; Nelson et al., 1992; Rosendahl,  
43 1987). The propagation and linkage of formerly isolated rift segments resembles the  
44 propagation and interaction of extension fractures on a micro-scale (e.g., Childs et al., 1995;  
45 Willemsse, 1997; Willemsse et al., 1996; Fig. 1a). Indeed, analytical solutions and models have  
46 been used to describe crack growth and to predict its direction (e.g., Macdonald and Fox,  
47 1983; Mills, 1981). Such cracks occur in a variety of materials over a vast order of magnitude  
48 in length scale from micro-scale cracks in glass to km-scale ridge interaction structures in  
49 oceanic crust (Pollard and Aydin, 1984; Fig. 1a).

50

51 Propagation and interaction of individual rift segments occur in continental rift systems at  
52 various styles and scales (Fig. 1b) and have been intensively studied over the years. The East  
53 African Rift System (EARS) constitutes a narrow rift with an Eastern and Western branch that  
54 propagate southward and northward, respectively (EARS; e.g., Ebinger et al., 2000; Morley  
55 et al., 1990; Nelson et al., 1992; Bonini et al., 2005; Bosworth, 1985; Brune et al., 2017; Corti

56 et al., 2019; Glerum et al., 2020; Heilman et al., 2019; Koehn et al., 2008; Kolawole et al.,  
 57 2018) comprising different sub-parallel deformed regions (inset Fig. 1c). On smaller scale,  
 58 interaction of segmented grabens has been studied for example in in the Canyonlands National  
 59 Park, Utah, a part of the Basin and Range wide rift (Allken et al., 2013; Trudgill, 2002; Schultz-  
 60 Ela and Walsh, 2002), where various styles of graben interaction are attributed to the  
 61 underlying strata (e.g., salt layer) or pre-existing weaknesses (Fig. 1d).

62



63  
64

65 **Figure 1:** Similar linkage structures occurring at a vast range of spatial scales. a) Propagation and linkage of segments at  
66 different scale from micro cracks in glass to linkage of oceanic ridge segments. Redrawn after Pollard and Aydin, (1984). b)  
67 Rift-interaction types investigated in this study. c) Rukwa Rift and Malawi rift along the Western Branch of the East African  
68 Rift System (EARS; inset). The two basins link obliquely via the Karonga Basin and form an i-type interaction zone. Rift axis  
69 redrawn after Kolawole et al., (2021). WB: Western Branch; EB: Eastern Branch of the EARS. d) Rift-related linked graben  
70 structures in the Canyonlands National Park, USA. Red rectangles mark areas with distinct interaction geometries (v-, i-, and  
71 y-geometries; see b) and text for detail). Redrawn after Allken et al., (2013).

72

73 Structural inheritance is thought to control nucleation and strain distribution along newly  
74 formed normal faults, as weak fabrics can precondition and weaken a heterogenous upper  
75 crust (e.g., Collanega et al., 2018; Heilman et al., 2019; Kolawole et al., 2018; Morley, 2010;  
76 Morley, 1999; Kolawole et al., 2021; Morley et al., 2004). Pre-existing weak fabrics may appear  
77 as large shear zones (Daly et al., 1989), suture zones along adjacent basement terranes (Corti,  
78 2012; Corti et al., 2007) or upper crustal fabrics. Resulting rift structures may form as initially  
79 isolated segments that propagate along strike, interact and evolve into continuous zones of  
80 deformation as they link (Nelson et al., 1992). Rift segments link through previously un-rifted  
81 interaction zones resulting in a characteristic geometry that persists during later rift stages  
82 (Nelson et al., 1992).

83

84 Recent strain accommodation in the Rukwa-North Malawi segment of the western branch of  
85 the EARS (Fig. 1c) shows dominant dip-slip faulting parallel to the border faults (Kolawole et  
86 al., 2018; Morley, 2010) driven by the reactivation of pre-existing basement fabrics (Heilman  
87 et al., 2019). There, the concentration of seismicity in the SE and NW of the Rukwa and  
88 Northern Malawi Rift, respectively suggest subsequent propagation and linkage of the rift  
89 segments with a flip in the boundary fault polarity near the interaction zone (Heilman et al.,  
90 2019 and references therein).

91

Deleted: with time

93 Pre-existing structures as well as fault interaction across multiple scales disturb the [regional](#)  
94 stress orientation (Morley, 2010; Oliva et al., 2022). In return, stress re-orientations within  
95 and adjacent to rift segments influence the style of progressive deformation. Ultimately, stress  
96 re-orientation may even favor pure dip-slip behavior even for extensional faults with an  
97 oblique orientation to the regional extension (e.g., Morley, 2010; Corti et al., 2013; Morley,  
98 2017; Philippon et al., 2015). This interplay between pre-existing structures and local re-  
99 orientation of the regional stress field affects how propagating rift segments interact. Under  
100 favorable conditions, it may even cause deflection of propagating rift segments (Nelson et al.,  
101 1992).

Deleted: regionally inferred

102  
103 Rift propagation and segment interaction has been investigated by analog modelling studies  
104 that examined linkage of two segments across a transfer zone (e.g., Zwaan et al., 2016;  
105 Zwaan and Schreurs, 2017; Corti, 2012; Acocella et al., 1999; Bellahsen and Daniel, 2005).  
106 Bellahsen and Daniel (2005) studied the control of existing faults on new fault growth under  
107 multiphase extension. They suggested that pre-existing faults may disturb the local stress field  
108 and impede linkage of newly forming faults which also occurs in natural examples of  
109 multiphase extension (Duffy et al., 2015). Such stress deflections [due to the vicinity of pre-](#)  
110 [existing faults](#) have been reported and studied in natural settings such as the North Malay  
111 Basin, Thailand, (Tingay et al., 2006; Tingay et al., 2010). While analog experiments are an  
112 effective tool to simulate mechanical (brittle and ductile) deformation processes, accessing  
113 information about stresses is challenging. In contrast, numerical modelling experiments  
114 provide direct access to element-wise stress tensors that can be interpreted in terms of stress  
115 regimes and orientations under extension (Brune and Autin, 2013; Duclaux et al., 2020).  
116 Despite the impact of stress distribution on faulting and rift segment interaction, only recently  
117 numerical studies made use of it to gain further insights into rift evolution and continental  
118 break-up (e.g., Glerum et al., 2020; Mondy et al., 2018). However, these studies mostly focus

Deleted: due to the vicinity of pre-existing faults

Deleted: occurring in continental rifts in 3D

122 on larger-scale deformation to evaluate stresses over the entire time span of rifting up to  
123 continental break-up.

124

125 Here we use crustal-scale analog and numerical models to investigate rift propagation and  
126 strain localization in early rifting stages when rift segments interact. Both types of models  
127 document enigmatic rift segment deflection when two sub-parallel rift segments propagate  
128 approximately in the same direction and compete for linkage with an opposingly propagating  
129 segment. To understand the reason for rift segment deflection, we analyze the stress  
130 distribution in early rifting stages and its interplay with strain localization that initiates above  
131 pre-existing structures. Our experiments show that relatively simple rift segment interactions  
132 can cause locally complex stress patterns that deviate from the regional stress field. Such  
133 stress re-orientations occur in transient stages and can change over time and with progressive  
134 deformation due to changes in material strengths.

135

Deleted: subsequent

137 **2. Analog model**

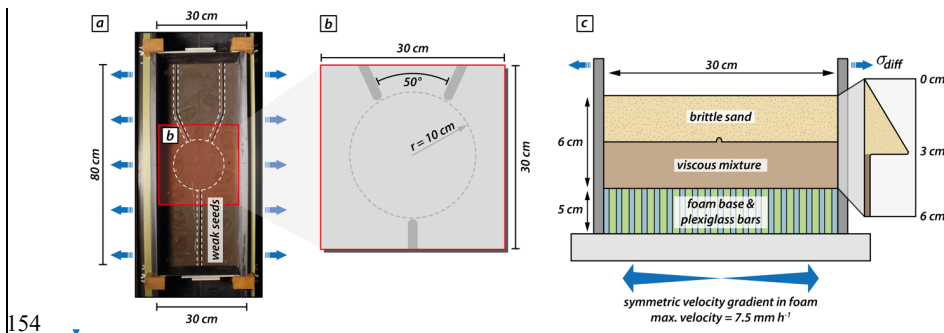
138 The presented analog modelling experiment shows unexpected features such as rift deflection.  
139 It motivates our numerical study, and we use the analog model as a reference for examining  
140 strain and stress distribution in numerical experiments.

141

142 **2.1. Analog model setup**

143 For the analog reference model, we use a simplified two-layer crustal scale setup with a brittle  
144 and a viscous material to simulate upper crustal brittle faulting and lower crustal viscous  
145 deformation, respectively. The base of the model consists of a set of alternating plexiglass  
146 and foam bars which are compressed prior to the model preparation by two mobile sidewalls  
147 (Fig. 2a). During the experiment the computer-controlled sidewalls extend and provide a  
148 symmetric velocity gradient as the model base expands and the model vertically thins. For  
149 monitoring the surface deformation evolution, we use a stereoscopic camera setup to take  
150 top view photos and stereo image pairs every 60 s for quantitative deformation analysis by  
151 means of 3D stereo Digital Image Correlation (Adam et al., 2005). The model was scanned  
152 every 20 min in a medical XRCT scanner for gaining insights on internal model evolution.

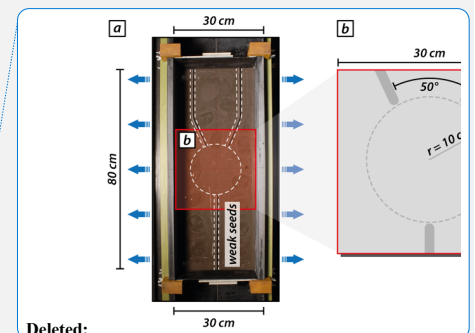
153



154  
155

156 **Figure 2:** Analog modelling setup. a) Top view of the experimental apparatus with two mobile side walls that extend  
157 orthogonally. The entire model comprises an area of 80 x 30 cm and three viscous seeds are placed on top of the viscous layer  
158 before sieving in the brittle sand layer. The central model part where propagating rift segments interact contains no seeds.

Deleted: extension



Deleted:

161 *b) Zoom in of the seed configuration into the analyzed model area (i.e., 30 x 30 cm). The two competing seed segments form*  
162 *an intermediate angle of 50°. The model center contains an area with a radius of 10 cm where weak seeds are absent. c)*  
163 *Sketch of the model cross section. The model setup consists of a brittle sand layer representing the upper brittle crust on top*  
164 *of a viscous mixture of PDMS and corundum sand imitating the lower ductile crust.*

165

## 166 **2.2. Model geometry, rheological layering, and material properties**

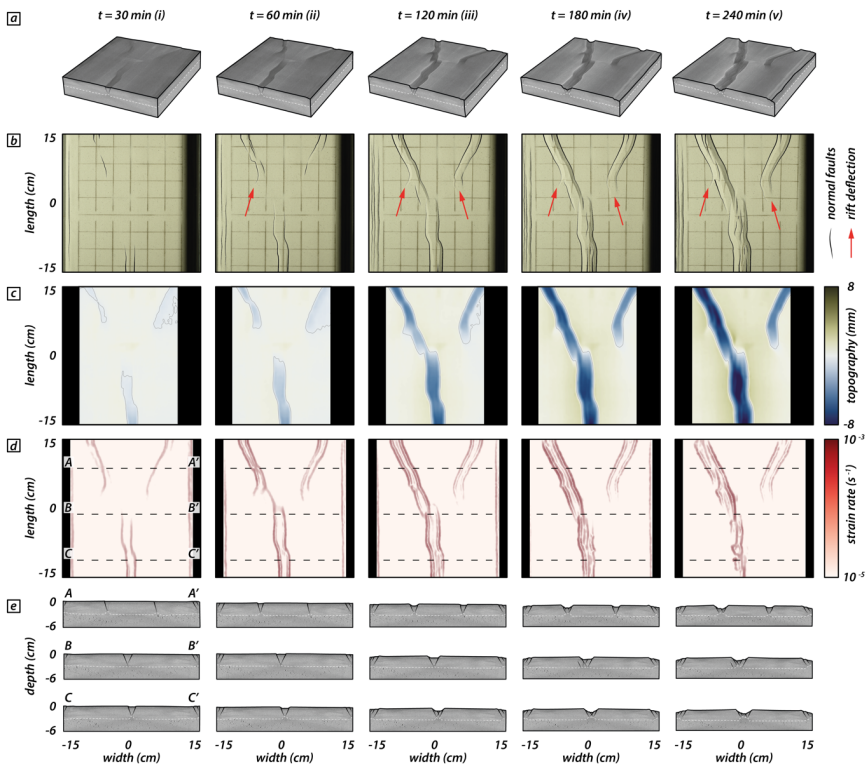
167 For simulating upper crustal deformation, we use dry quartz sand with a bulk density of 1560  
168 kg m<sup>-3</sup> and an internal friction coefficient of 0.72 (Schmid et al., 2020a). For the lower viscous  
169 model part, we use a quasi-Newtonian PDMS/corundum sand mixture (weight ratio 1:1) with  
170 bulk density of 1600 kg m<sup>-3</sup> and a viscosity of  $\sim 1 \times 10^5$  Pa s (Zwaan et al., 2018). Hence, the  
171 brittle-viscous setup has a density gradient that avoids density instabilities and spontaneous  
172 upwelling of the viscous layer. The model features viscous rods placed on top of the viscous  
173 model layer before sieving in the quartz sand (Fig. 2). These rods act as mechanically weak  
174 seeds and localize faulting in the upper brittle model domain. The used seed configuration  
175 includes three individual seed segments. The model includes a y-seed configuration with one  
176 seed segment perpendicular to the extension direction on one side (hereafter called frontal  
177 segment) whereas on the opposing side of the model center two obliquely placed seeds  
178 (hereafter called rear segments) form an intermediate angle of 50° (Fig. 2; see also Fig. 1b,d).  
179 The three seed segments hypothetically merge at the model center. However, we exclude  
180 weak seeds in an area with a radius  $r = 10$  cm around the model center to allow free  
181 interaction of the propagating rift structures (Fig. 2b). The analog model comprises an initial  
182 area of 80 cm by 30 cm and has a total thickness of 6 cm (each layer 3 cm) which represents  
183 a 30 km thick continental crust. In accordance with the numerical setup, the effectively  
184 analyzed model area is restricted to 30 x 30 cm. The mobile sidewalls move with an extension  
185 velocity of 5 mm h<sup>-1</sup> each (totaling in 10 mm h<sup>-1</sup>), which results in a maximum extension of  
186 40 mm at the final model stage after 4h.

187



188 **2.3. Analog model results**

189 In the analog model three different rift segments initiate above the weak seeds and propagate  
190 toward each other. Thereby, the two rear segments compete for linkage with the frontal  
191 segment. After 30 min (i.e., 5 mm extension; Fig. 3(i)), brittle deformation localizes along two  
192 rift boundary faults forming the frontal rift segment. Rifting in the rear segments localizes first  
193 along right-dipping rift boundary faults and after 60 min (i.e., 10 mm extension; Fig. 3(ii))  
194 both rear segments develop a set of two conjugate rift boundary faults (Fig. 3a,b (ii)).  
195 Interestingly, instead of advancing straight forward, the fault tips deflect and propagate away  
196 from each other (Fig. 3b,d (ii)). This is partially due to the rift propagation over the area where  
197 no seeds are present where rifting perpendicular to the extension direction is favored.  
198 However, after 120 min (i.e., 20 mm extension; Fig. 3 (iii)) rift tips deflect and turn away from  
199 one another. Rift tips deflect from an initially oblique orientation and rotate into an inverted  
200 oblique direction (with respect to the extension direction). The frontal and the rear left rift  
201 segment propagate further and, as they approach one another, form an en-echelon basin that  
202 convergently overlaps with the frontal rift segment (Morley et al., 1990; Fig. 3b,d (iii)). After  
203 180 min (i.e., 30 mm extension; Fig. 3(iv)), intra-rift faults develop in the frontal and left rear  
204 rift segments. Note that strain rate is successively localized in the two fully linked rift segments  
205 whereas the right rear segment experiences minor strain rate values (Fig. 3d (iv)). At the final  
206 model stage (i.e., after 240 min and 40 mm extension; Fig. 3 (v)), the right rear segment  
207 propagated minimally with a rift tip turned away from the linked segments (Fig. 3b,d (v)). The  
208 fully linked frontal and left rear segments continuously accommodated displacement resulting  
209 in deeper rift structures compared to the abandoned right rear segment (Fig. 3c,e (v)).  
210



211  
 212  
 213 **Figure 3:** Analog modelling results documenting deflection of the right rear segment and cessation of faulting activity. Distinct  
 214 time steps (i.e., after 30 min and after every hour) show the model evolution. a) CT volumes of the investigated model domain  
 215 at distinct time steps. White dashed lines indicate the brittle-viscous interface. b) Top views and line drawings indicating  
 216 observable normal faults at the model surface. Red arrows indicate rift tips that deflect and turn away from one another. c)  
 217 Topography from digital elevation models of the model surface. d) Strain rates obtained from 3D stereo DIC. Black dashed  
 218 lines indicate positions of 3 transects through the CT volume. e) Rift transects A-A', B-B', and C-C'. White dashed lines indicate  
 219 the brittle-viscous interface.

220

### 221 3. Numerical modelling

222 We perform a series of numerical models to investigate rift linkage interaction and to analyze  
 223 occurring surface stresses. Similar to the analog experiment, the numerical model consists of  
 224 a two-layer crustal setup with laterally homogenous material layers where boundary-  
 225 orthogonal extension with constant velocity is applied.

### 226 **3.1. Numerical model setup**

227 We use the open source, finite-element code ASPECT to solve the extended Boussinesq  
228 equations of momentum, mass, and energy in combination with advection equations for each  
229 compositional field (Gassmüller et al., 2018; Glerum et al., 2018; Heister et al., 2017;  
230 Kronbichler et al., 2012; Rose et al., 2017; Glerum et al., 2020). Since the numerical models  
231 are motivated by the analog model, the two setups are designed in a similar way. To this aim,  
232 we employ a numerical setup where the rheologies of upper and lower crust are brittle and  
233 ductile, respectively, and independent of temperature just like in the analog model. However,  
234 the numerical models operate on the true scales of the continental crust over tens of  
235 kilometers and millions of years, while the analog model is a scaled, cm-sized representation  
236 that evolves on hour-scale. Additionally, the numerical setup applies maximum extension  
237 velocities at the side walls and extension velocities at the base that linearly increase from the  
238 center towards the model boundaries. In contrast, maximum extension velocities at the side  
239 walls in the analog model are achieved via compression of a basal foam plexiglass setup (prior  
240 to the model run) that extends homogeneously during the model run.

241  
242 The presented numerical experiments cover a rectangular cuboid domain of 150 km width  
243 and length in the horizontal x- and y-direction, respectively, and 30 km in depth along the  
244 vertical z-axis (Fig. 4a). The entire model domain is divided into 1.53 million hexahedral,  
245 second-order elements. For the upper 15 km of the model, we use a cell resolution of 750 m,  
246 with an additional refinement at the uppermost km which yields near-surface elements with a  
247 resolution of 375 m. The grid resolution for the lower 15 km of the model is 1500 m. At the  
248 left and right model sides, we apply a symmetrically distributed outflow velocity of  $\frac{1}{2} V_x = 5$   
249  $\text{mm yr}^{-1}$ , resulting in a total extension velocity of  $10 \text{ mm yr}^{-1}$  (Fig. 4a,b). After a total model  
250 time of 4 My, the model has therefore experienced a total extension of 40 km. While  $V_x$  is  
251 prescribed at the left and right model sides,  $V_y$  and  $V_z$  are left free. We compensate material

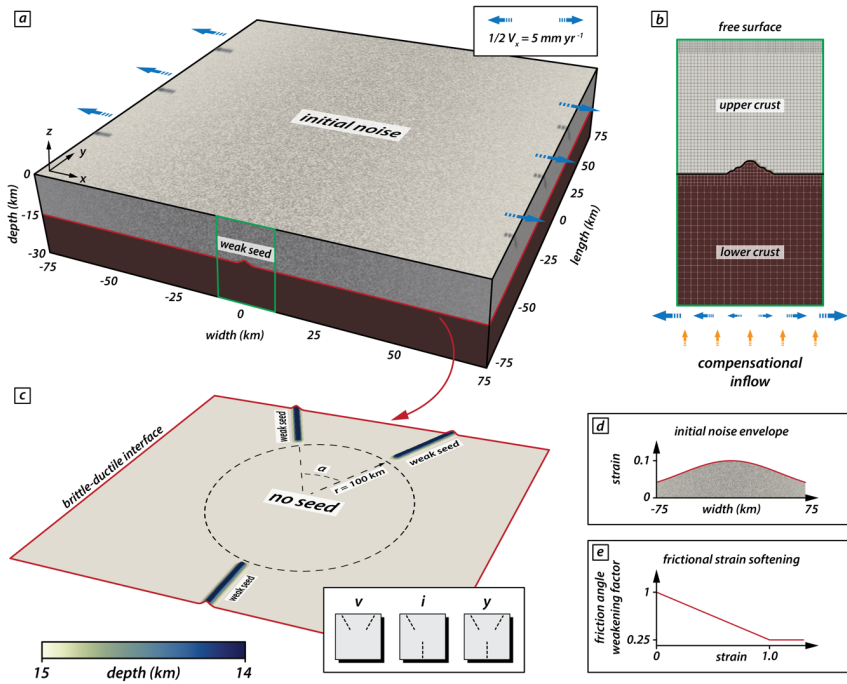
252 loss through the side boundaries by compensational inflow at the model base (Fig. 4b). The  
253 front and back lateral boundaries allow for free slip and the top of the model features a free  
254 surface boundary condition (Rose et al., 2017).

255

256 The model includes two rheological layers represented by compositional fields, namely a 15  
257 km thick visco-plastic upper crust with a density of  $2700 \text{ kg m}^{-3}$  and a 15 km thick iso-viscous  
258 lower crust with a density of  $2900 \text{ kg m}^{-3}$  and a constant viscosity of  $1 \cdot 10^{20} \text{ Pa s}$ . For the upper  
259 crust, the viscous viscosity is fixed to  $2 \cdot 10^{28} \text{ Pa s}$ , such that plastic deformation is always  
260 enabled. We introduce initial and dynamic mechanical weaknesses in the upper crust in two  
261 ways. (i) Mechanically weak seeds: At distinct positions near the brittle-ductile interface, the  
262 upper model layer is locally 10% thinned and the lower model layer elevates like the viscous  
263 weak seeds in the analog model setup. These mechanical seeds weaken the upper crustal  
264 strength and localize brittle faulting. Our experiments include three different seed  
265 configurations: v, i, and y (Fig. 4c; see also Fig. 1b-d), where seeds within a central model  
266 area (i.e.,  $r = 100 \text{ km}$ ) are absent. For each configuration, the rear seeds form an intermediate  
267 angle of  $10^\circ$ ,  $30^\circ$ , or  $50^\circ$ . (ii) Friction softening: For each element, an initial plastic strain value  
268 of 0 (resulting in strong material) to 0.1 (weaker) is randomly assigned and reduces the  
269 maximum friction angle of  $26.56^\circ$  by a maximum of 10%. This reflects the structural  
270 heterogeneity of natural settings and allows for more randomized strain patterns in the central  
271 model domain where the mechanical seeds are absent. The initial plastic strain noise is  
272 distributed over the entire model width with an amplitude following a Gaussian curve parallel  
273 to the extension direction that is repeated along the model length (y-direction, Fig. 4d). During  
274 continuous extension, the effective friction angle linearly reduces to 25% of the maximum  
275 friction angle (i.e., to  $6.64^\circ$ ) for plastic strain between 0 and 1 while it remains constant at  
276  $6.64^\circ$  for plastic strains  $> 1$  (Fig. 4e). This corresponds to a reduction of the effective friction

Deleted: and the horizontal  $V_x$  component increases linearly from the model center towards the lateral model boundaries (Fig.

280 coefficient from 0.5 to 0.12. The cohesion of the upper crust remains constant at  $5 \cdot 10^6$  Pa for  
 281 all conducted experiments.  
 282



283 **Figure 4:** Numerical model setup for iso-viscous models. a) The model domain comprises a volume of 150 x 150 x 30 km. Blue  
 284 arrows indicate the applied boundary-orthogonal extension. The green rectangle indicates the position of the zoom-in in b).  
 285 The red line indicates the initial depth of the brittle-ductile interface (as defined by the interface between the two rheological  
 286 layers) indicated in c). b) Initial conditions and mesh refinement (arrows not to scale). c) Position and configuration of the  
 287 mechanical weak seeds at the brittle-ductile interface. The setup comprises an area with radius  $r = 100 \text{ km}$  where no weak  
 288 seeds are present. Three different seed configurations refer to y-, i-, and v-models (see text for details). d) Initial amplitude of  
 289 strain along the x-axis. The Gaussian distribution is constant along the y-axis; also see grey shade in a). Note that while the  
 290 strain amplitude follows a Gaussian distribution, the location of the initial strain is random. e) Linear weakening with strain  
 291 applied to the friction angle.  
 292  
 293

294

295 **3.2. Model limitations**

296 Just like the analog model (Sec. 2), our crustal scale two-layer numerical setup does not  
297 comprise a lithospheric mantle layer and no asthenosphere. Further, the iso-viscous setup  
298 does not account for a temperature-dependent viscosity. However, we focus on an early rifting  
299 phase where the influence of the deforming mantle lithosphere can be neglected. The crustal-  
300 scale setup strongly limits the computational effort for calculating deformation in 3D (Allken  
301 et al., 2011, 2012; Katzman et al., 1995; Zwaan et al., 2016) and hence, our simplifications  
302 allow for a higher model resolution; a necessity to depict early stages of rifting and the  
303 coalescence of brittle deformation. Several alternative model runs have been performed  
304 including a temperature- and pressure-dependent viscosity. Those tests reproduced first-order  
305 features (i.e., strain rates, rift geometry and stress distribution) of the presented models in  
306 this study, which further justified the choice of a simplified iso-viscous setup. Note that we  
307 apply frictional softening as a function of strain within each cell. For simplicity, we do not  
308 include normalization accounting for cell size (Lavie et al., 2000) nor viscoplastic  
309 regularization techniques (Duretz et al., 2019; Jacquy and Cacace, 2020). Moreover, our  
310 model does not include the influence of melting or magma intrusions nor sedimentation and  
311 erosion.

312

313 **3.3. Post-processing**

314 Numerical models pose the advantage that they grant direct access to stress tensors of each  
315 individual cell. We exploit this opportunity by investigating surface stresses to deduct the  
316 stress regime and the effect of different seed configurations on stress distribution. ASPECT  
317 provides post processors that calculate the magnitude and orientation of the maximum  
318 horizontal stresses and the Regime Stress Ratio (RSR) (Glerum et al., 2020). This stress  
319 regime characterization is calculated according to the scheme of the World Stress Map  
320 (Zoback, 1992). The RSR value maps possible stress regimes to an interval between 0 and 3.

321 For isotropic and homogenous materials, the standard rules of Andersonian faulting are  
322 applied (Anderson, 1905). For RSR values  $< 1$ , faulting occurs in an extensional stress regime  
323 whereas for RSR values  $> 2$  compressive stress regimes generate thrust faults. Strike-slip  
324 faults occur for values  $1 \geq \text{RSR} \geq 2$ . We extract data of maximum horizontal compressive  
325 stress together with the stress regime and investigate them in areas where the strain rate  
326 exceeds a threshold of  $10^{-16} \text{ s}^{-1}$  and deformation occurs. For visualization, surface stresses  
327 from an originally unstructured grid are resampled on an equidistant grid.

328

### 329 **3.4. General model evolution of the reference model**

330 In this section we describe the numerical modelling results focusing particularly on the general  
331 evolution of our reference model with a y-seed configuration and an intermediate seed angle  
332 of  $50^\circ$  (Figure 5). At the early stage (i.e., after 0.5 million years), three distinct rift segments  
333 develop above the initial seed positions bounded by a pair of conjugate rift boundary faults  
334 (Fig. 5a (i)). This early stage is characterized by a symmetric evolution of the two competing  
335 rear segments, which results in a symmetric subsidence inside of the graben structures (Fig.  
336 5b (i)). For each rift segment, faulting activity is localized along the rift boundary faults. In  
337 the central model domain, however, strain rates depict a more distributed deformation pattern  
338 with multiple minor faults (Fig. 5c (i)). Note that the two rear segments propagate and show  
339 curved fault segments that initially deflect and turn away from each other resulting in rift  
340 segments with a curved geometry expressed in the topography (Fig. 5b (i)), similar to the rift  
341 evolution in the analog model. Once they overlap with the propagating frontal segment, faults  
342 symmetrically curve inwards and towards the frontal segment. The change from localized  
343 strain rates above the seeds to distributed strain rate patterns in the central model domain is  
344 best seen in transects (Fig. 5d (i)).

345

346 After the first million years, deformation has prominently localized along the left of the two  
347 rear segments and along the frontal segment (Fig. 5a,c, (ii)). While deformation in the frontal  
348 segment is localized along the rift boundary faults, inward migration occurred in the left rear  
349 segment with developing intra-rift faults and only the left-dipping rift boundary fault active.  
350 Similarly, the right rear segment shows faulting along the right-dipping rift boundary fault but  
351 activity along intra-rift faults is lacking. In the central model domain, formerly distributed  
352 deformation localized between the frontal and left rear rift segment (Fig. 5d (ii)). While strain  
353 rates indicate a shift from a symmetric to an asymmetric deformation phase, topography is  
354 still symmetric which implies that the shift is imminent and has not affected the topography  
355 after the first million years (Fig. 5b (ii)).

356

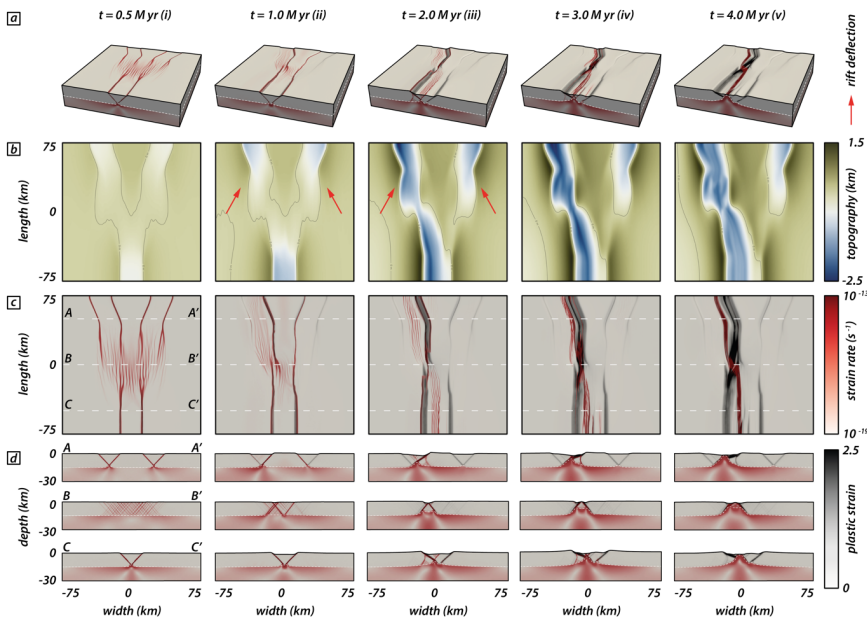
357 After two million years, deformation is entirely localized along the frontal and left rear  
358 segment. Only the right-dipping rift boundary fault of the frontal segment is active and inward  
359 migration led to a set of pervasive intra-rift faults (Fig. 5a,c (iii)). The left rear segment depicts  
360 a similar deformation pattern as in the previous step, but strain mainly accumulates along the  
361 left-dipping rift boundary fault causing an asymmetric graben geometry (Fig. 5d (iii)). Note  
362 that, after two million years, fault activity along the right rear segment completely ceased with  
363 no further strain accumulation visible (Fig. 5a,c,d (iii)). The topography reflects this completed  
364 switch from a symmetric to an asymmetric deformation stage with enhanced subsidence along  
365 the frontal and left rear segments and their linkage throughout the central model domain (Fig.  
366 5b (iii)).

367

368 With ongoing extension, deformation subsequently localizes along the axial rift zone that links  
369 the frontal and left rear segments (Fig. 5a,c,d (iv,v)) and faulting activity along rift boundary  
370 faults ceases. The linked structure reaches maximum depth inside of the rift after three million  
371 years. After four million years, however, the basin experiences minor uplift due to increase



372 upward motion of the underlying viscous material (Fig. 5d (iv,v)). Note that the basin depth  
 373 of the right rear rift segment remains stable after two million years and does not experience  
 374 further subsidence nor uplift.  
 375



376  
 377 **Figure 5:** Modelling results of the reference model documenting cessation of fault activity along the right rear segment while  
 378 the left rear and frontal segments link. Distinct time steps show the model evolution. a) Model box showing logarithmic strain  
 379 rates (red) and plastic strain (black) in the brittle and viscous model domain. White dashed lines indicate the brittle-viscous  
 380 interface. b) Top views showing the model topography. Red arrows indicate rift tips that deflect and turn away from one  
 381 another. Black lines refer to the zero-elevation height. c) Top views of the model showing strain rates (red) and corresponding  
 382 plastic strain (black) at distinct model run times. White dashed lines correspond to the three rift transects A-A', B-B', and C-C'  
 383 in subfigure d). d) Rift-axis perpendicular transects A-A', B-B', and C-C' parallel to the extension direction.  
 384

385  
 386 **3.5. Early localization patterns for v-, i-, and y-seeds**

387 To investigate the influence of different seed configurations, we compare v- (Fig. 6a-c), i-  
 388 (Fig. 6d-f), and y-seed (Fig. 6g-i) configurations for different intermediate angles (i.e., 10°,  
 389 30°, and 50°) at an early stage after 0.5 million years. y- and i-seed configurations provide a

390 setup where rift structures opposingly propagate towards the model center where rift linkage  
391 eventually occurs. In contrast, rift structures in the v-seed configuration propagate  
392 approximately in the same direction, which has a consequence on the overall strain rate  
393 distribution.

394

395 The early stage in v-seed experiments (Fig. 6a-c) is characterized by a zone of localized and  
396 distributed deformation in the rear and frontal part of the experiments, respectively. The  
397 transition from localized to distributed deformation occurs where the two competing rift  
398 segments deflect and rotate away from one another. Note that the fault deflection successively  
399 decreases towards the left and right model sides, where faults strike perpendicular to the  
400 extension direction. This is consistent with observations for experiments with a y-seed  
401 configuration. However, there the two competing rear segments rotate back and eventually  
402 bend towards the propagating frontal segment (Fig. 6g-i).

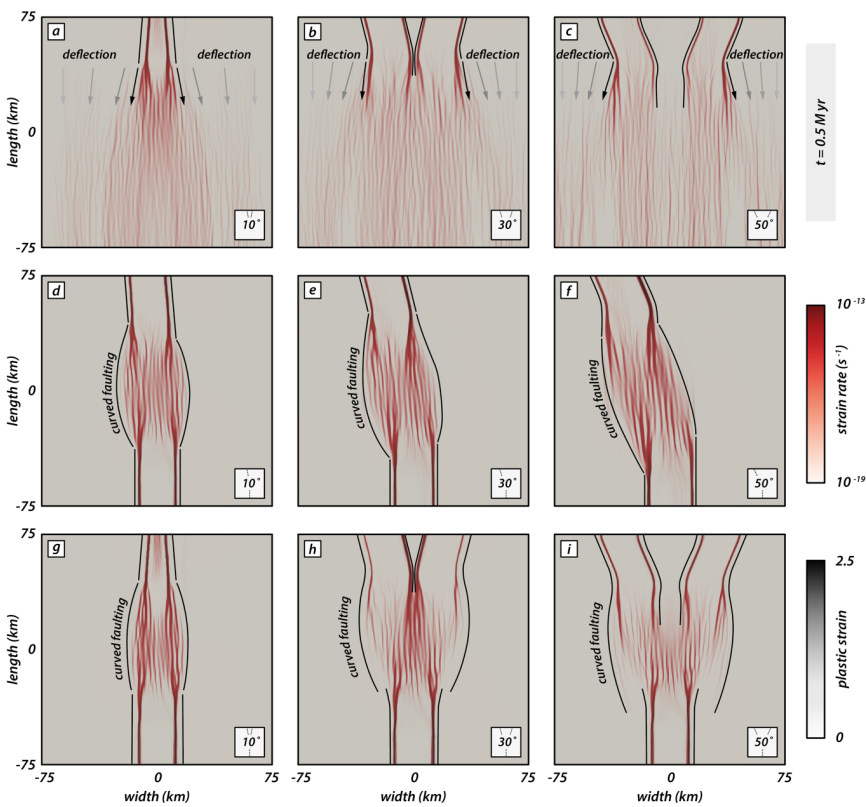
403

404 For experiment with a i-seed configuration (Fig. 6d-f) two opposingly propagating rift branches  
405 form. Since the right rear segment is absent, both opposingly propagating rift segments link  
406 in the model center where deformation is distributed onto intra-rift faults. The overall strain  
407 rate field is localized, and no strain rate deflection occurs.

408

409 Models with a y-seed configuration (Fig. 6g-i) depict a strain rate pattern where deformation  
410 is localized along rift boundary faults at the model margins where seeds are present and a  
411 distributed en-echelon strain rate pattern in the model center. Note that for the model with  
412 an intermediate angle of  $10^\circ$  the two competing rear segments are close enough resulting in  
413 a zone where strain is localized along only one rift boundary fault per rift segment (i.e.,  
414 outward-dipping faults with respect to the model box) that overlap and form a central graben  
415 with minor intra-rift faults. For larger intermediate angles, two individual rift segments

416 (bounded by two rift boundary faults) form that propagate towards the model center. While  
 417 the strain rate pattern due to the competing rear segments is identical for experiments with  
 418 a y- and v-seed configuration, the additional frontal segment in experiments with a y-seed  
 419 configuration causes localization of strain rates in a single rift branch bounded by two rift  
 420 boundary faults. This contrasts with the v-seed configuration where strain rates in the frontal  
 421 model domain occur distributed over the entire model domain (Fig. 6a-c).  
 422



423  
424

425 **Figure 6:** Types of rift segment linkages depending on the seed configuration at an early phase after 0.5 million years. Model  
 426 top views show strain rates (logarithmic) and plastic strain in red and black colors, respectively. a-c) v-seed configuration for  
 427 intermediate angles of 10°, 30°, and 50°. d-f) i-seed configuration for intermediate angles of 10°, 30°, and 50°. g-i) y-seed  
 428 configuration for intermediate angles of 10°, 30°, and 50° (reference model). Black lines confine deformed areas. For models

429 *with a v-seed configuration (a-c), competing rift segments deflect away from each other resulting in a fan-shaped geometry.*  
430 *Note that fault strike successively re-orientates into an orientation perpendicular to the extension direction towards the left and*  
431 *right model sides. Curved faulting occurs in models with an i- and y-seed configuration (d-j) where rift segments interact.*

432

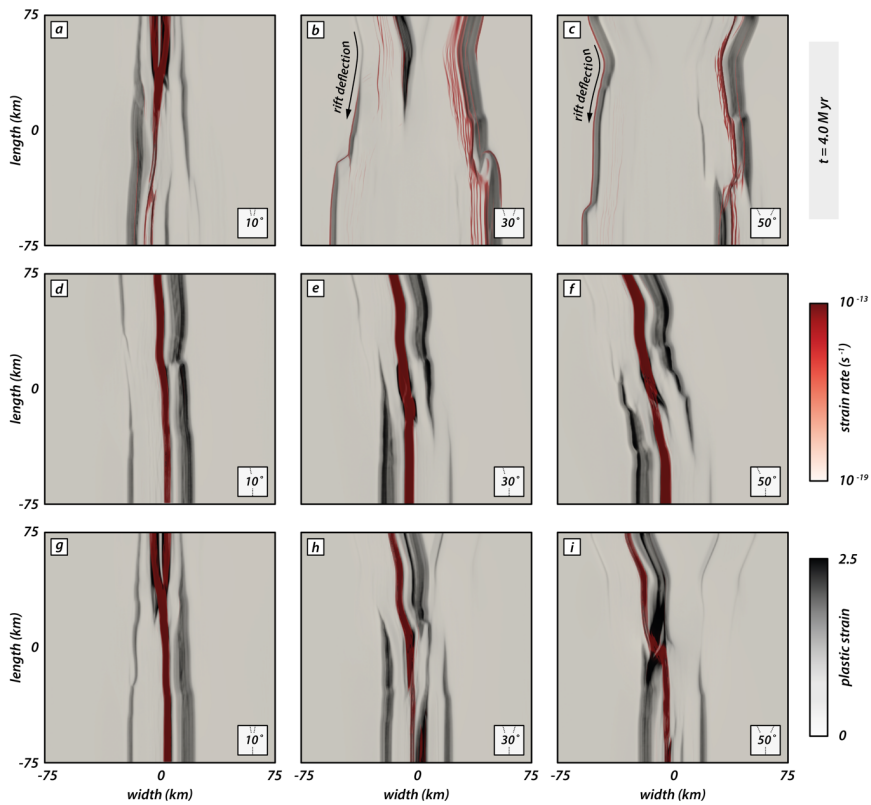
### 433 **3.6. Final rift geometry and localization patterns for v-, i-, and y-seeds**

434 The final model stage after four million years best illustrates differences in rift geometry  
435 between the models with different seed geometry and an intermediate angle (Fig. 7). Rift  
436 deflection is well visible in v-seed models (Fig. 7 a-c) and most prominent in experiments with  
437 a larger intermediate angle (Fig. 7b,c). Above the seeds, two short individual rift segments  
438 form bounded by a pair of conjugate rift boundary faults. However, as the rifts propagate  
439 towards the model center, strain is mainly accommodated along the boundary faults that dip  
440 towards the model center. Hence, the larger part of the model subsides uniformly and builds  
441 a broad rift zone confined by two large boundary faults. When the two rift segments  
442 propagate, they deflect and turn away from one another resulting in a gradually wider rift.  
443 For intermediate angles of 30° and 50°, both competing rift segments show active faulting  
444 along intra-rift faults in the rear model part, but a zone of continuous faulting activity has  
445 developed along the right side of the rift.

446

447 Models with an i-seed configuration show a continuous and straight rift geometry for all  
448 intermediate angles (fig. 7d-f). For an intermediate angle of 10°, the rift structure is nearly  
449 orthogonal with respect to the extension direction. Note that most plastic strain is  
450 accommodated along the left-dipping rift boundary fault (Fig. 7d). For larger intermediate  
451 angles, the rift subsequently experiences more segmentation with small left stepping  
452 segments towards the rear model part (Fig. 7e,f). Strain accommodation occurs mainly on the  
453 right-dipping rift boundary fault for the frontal model part and switches to the left-dipping  
454 boundary fault in the rear model part.

455



456

457 **Figure 7:** Influence of seed configuration on the final rift geometry after 4 million years. Strain rates (logarithmic) and plastic  
 458 strain are indicated by red and black colors, respectively. a-c) v-seed configuration for intermediate angles of 10°, 30°, and  
 459 50°. d-f) i-seed configuration for intermediate angles of 10°, 30°, and 50°. g-i) y-seed configuration for intermediate angles  
 460 of 10°, 30°, and 50° (reference model).

461

462 The most prominent difference occurs in models with a y-seed configuration and various  
 463 intermediate angles. For an intermediate angle of 10°, the final rift geometry resembles that  
 464 of a continuous straight rift segment (Fig. 7g). Both competing rear seeds are close enough  
 465 such that they build one rift system rather than two distinct branches. For y-seed models with  
 466 a larger intermediate angle (Fig. 7h,i), two individual rear rift segments form and compete for  
 467 linkage with the frontal rift segment. Plastic strain well illustrates the asymmetric strain

468 accommodation focused along the left-dipping rift boundary fault of the left rear segment,  
469 whereas the right rear segment only experienced minor strain accommodation (Fig. 7h,i). In  
470 both cases, high strain rates are localized in the axial rift zone and witness activity along the  
471 linked frontal and left rear segments.

472  
473 Note that all experiments with an intermediate angle of  $10^\circ$  (Fig. 7a,d,g) form continuous  
474 straight rift segments, regardless of the seed configuration. Additionally, the final rift geometry  
475 for  $\gamma$ - and  $\nu$ -seed configurations for an intermediate angle of  $10^\circ$  is similar with a gently wider  
476 rift in the frontal model part (Fig. 7a,g). In contrast, for  $i$ -seed configurations the rift width is  
477 similar along the entire length with a minor lateral offset (Fig. 7d). Strain rates are localized  
478 in the axial rift zone throughout the entire model length forking into two close zones in the  
479 rear end where the competing seeds are located.

480

### 481 **3.7. $S_{Hmax}$ evolution with progressive deformation**

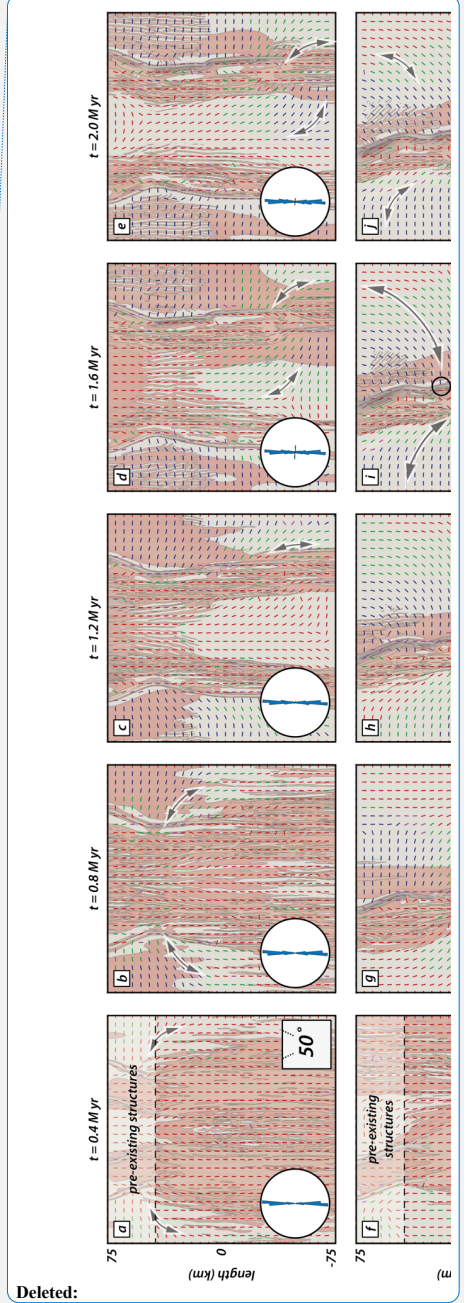
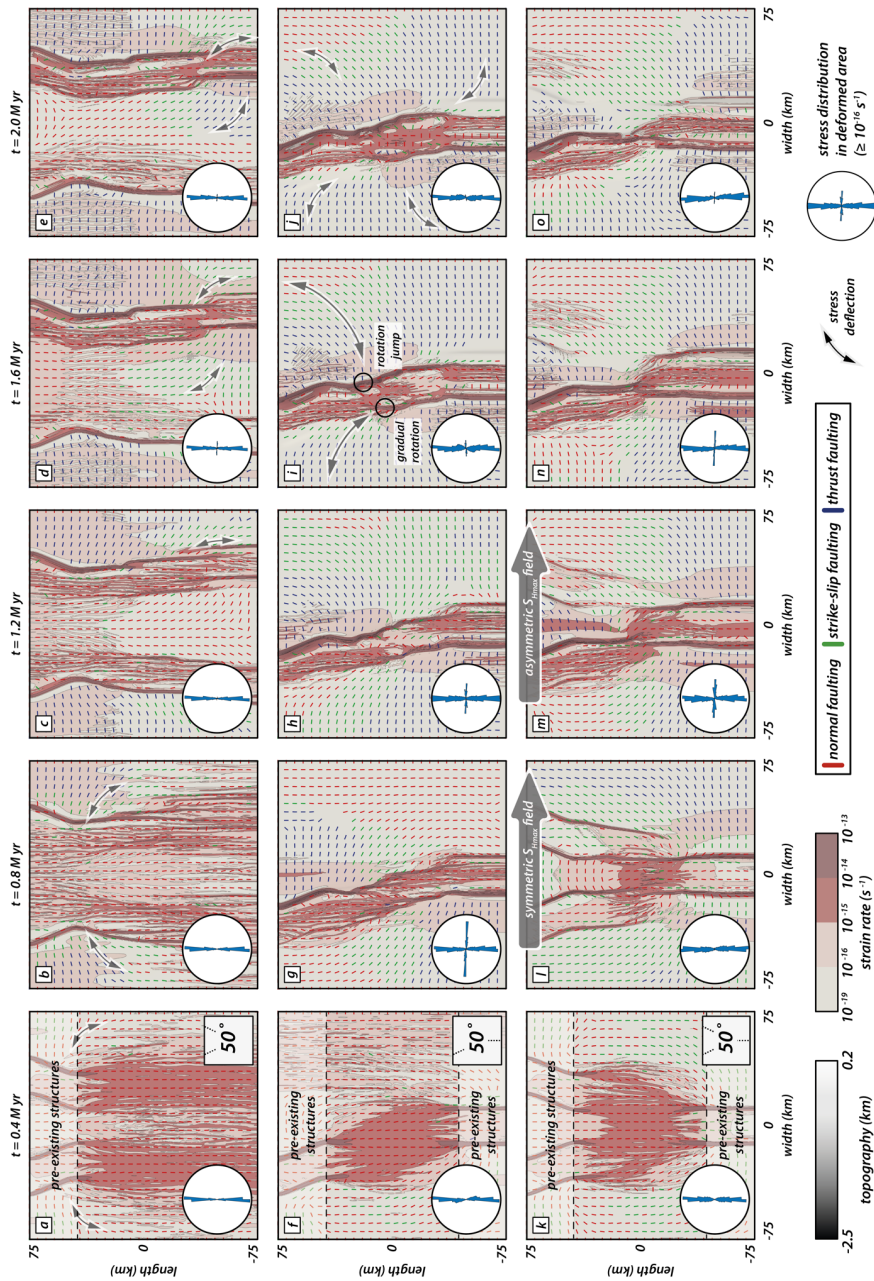
482 In this section we present the distribution and orientation of the maximal horizontal  
483 compressive stress component  $S_{Hmax}$  with progressive rift evolution and segment linkage. We  
484 focus on models with  $\nu$ -,  $i$ -, and  $\gamma$ -seed configurations and an intermediate angle of  $50^\circ$  (Fig.  
485 8; see also supplementary Figures S1-S3) distinguishing between model zones with pre-  
486 existing structures (i.e., weak seeds) and a central zone where material strength is isotropic.

487

488 Our models depict two distinct phases within the first two million years: early strain  
489 accommodation over a wider model domain followed by strain localization and linkage of  
490 propagating rift segments (see also supplementary Figures S4-S6). Consequently, we focus  
491 on  $S_{Hmax}$  in the first two million years of deformation and its effect on rift propagation. Figure  
492 8 shows the orientation of  $S_{Hmax}$  and the stress regime based on the common color scheme of  
493 the World Stress Map (Heidbach et al., 2018). Note that  $S_{Hmax}$  orientation and the stress regime

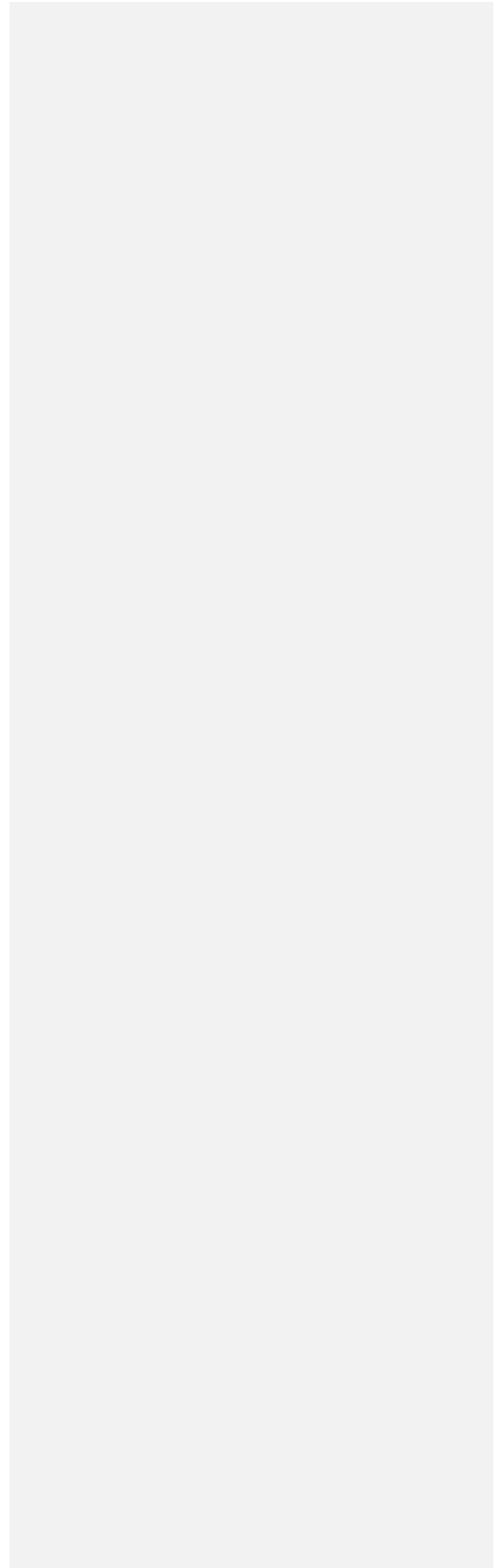
494 alone do not suffice to discriminate between locations where stresses exceed crustal strength  
495 and faulting occurs. Strain rate values provide further necessary information, and we use a  
496 threshold of  $10^{-16} \text{ s}^{-1}$  that splits the model into locations of active deformation (i.e.,  $\geq 10^{-16} \text{ s}^{-1}$ )  
497 and tectonically inactive domains (i.e.,  $< 10^{-16} \text{ s}^{-1}$ ).

498



Deleted:





502 **Figure 8:** Interplay of rift localization and surface stresses. Top views show the distribution of the maximum horizontal  
503 compressive stress component  $S_{Hmax}$  (not scaled to the magnitude) in models with an intermediate angle of  $50^\circ$  at early  
504 deformation stages (i.e., until 2 million years). a-e) v-seed configuration. f-j) i-seed configuration. k-o) y-seed configuration.  
505 Black colors refer to topographic elevation and red colors mark zones where strain rates exceed a threshold of  $10^{-16} s^{-1}$ . Color  
506 coding for the stress regime marks normal, strike-slip, and thrust faulting in red, green, and blue, respectively, using the  
507 common color scheme of the World Stress Map (Heidbach et al., 2018). Black arrows highlight stress deflection of  $S_{Hmax}$ . Rose  
508 diagrams show the distribution of  $S_{Hmax}$  orientation in zones where active faulting occurs (i.e., strain rate  $\geq 10^{-16} s^{-1}$ ). Large  
509 grey arrows for the y-seed configuration mark the change from a symmetric to an asymmetric  $S_{Hmax}$  distribution.

Deleted: Elements where the stress regime is non-defined are marked purple. ...

510

### 511 **3.7.1. Effect of $S_{Hmax}$ re-orientation on rift propagation of competing rift** 512 **segments (v-seed models)**

513 Early stages in our numerical experiments are characterized by rift deflection and curved fault  
514 traces in the model center where rift segments interact (see Fig. 6). Hereafter, we refer to  
515 that phenomenon as arcuate faulting. Arcuate faulting mainly occurs in experiments with  
516 larger intermediate angles ( $>10^\circ$ ) in early stages (Fig. 6), especially if two competing rift  
517 segments are present (v-, and y-seed configurations). Moreover, we have shown that  
518 deflection of propagating rifts occurs when deformation is symmetrically distributed along  
519 both competing rift branches. This is clearly visible for the v-seed configuration (Fig. 8a-e).  
520 Assuming orthogonal extension and isotropic material properties,  $S_{Hmax}$  is expected to align  
521 perpendicular to the extension direction producing pure dip-slip normal faults (Anderson,  
522 1905). However, the model shows an immediate  $S_{Hmax}$  re-orientation at early deformation  
523 stages (i.e., after 0.4 million years; Fig. 8a) from a N-S to a E-W orientation in the vicinity of  
524 the underlying weak seeds such that dip slip faults are favored over oblique-slip faults with a  
525 strike-slip component. With progressive extension (Fig. 8b-e),  $S_{Hmax}$  re-orientations  
526 successively propagate into the isotropic zone without pre-existing structures, concomitant  
527 with the rift propagation. Consequently, the position of the front where stress rotation occurs  
528 propagates over time resulting in the deflection of the propagating rift arms away from each  
529 other.

530

533 There is a distinct difference between stress deflection along weak structures and E-W  
534 deflections of  $S_{Hmax}$  in zones where strain rates are below the set threshold of  $10^{-16} \text{ s}^{-1}$ . The v-  
535 seed configuration shows localized strain accumulation along one rift boundary fault per  
536 segment (i.e., the outer one) resulting in a rift zone with a broad graben system that subsides  
537 (Fig. 8e).  $S_{Hmax}$  re-orientation inside of the graben is in parts identical to the E-W orientation  
538 of  $S_{Hmax}$  outside of the graben. While local  $S_{Hmax}$  rotations may be explained by small  
539 differences in the maximum and intermediate principal stress components, such E-W stress  
540 re-orientation in our model occurs systematically and suggest that this feature reflects the  
541 influence of the strength anisotropy (Morley, 2010). The initial  $S_{Hmax}$  deflection near weak  
542 structures locally favors dip-slip faulting but also has regional influence on the overall stress  
543 regime.

544

### 545 **3.7.2. $S_{Hmax}$ evolution in sub-parallel rift segments (i-seed models)**

546 During the early stage (i.e., after 0.4 million years, Fig. 8f), the distribution of  $S_{Hmax}$  resembles  
547 the distribution from the v-seed configuration described in the previous section. Stress  
548 deflection mainly occurs in zones where a weak fabric is present.  $S_{Hmax}$  values in the central  
549 zone rotate by a small amount and reflect arcuate faulting (see Fig. 6). Since the two rift  
550 segments propagate in opposing directions, linkage is efficient and localizes in a short time  
551 (Fig. 8f-j).  $S_{Hmax}$  values deflect accordingly along propagating faults, which affects the entire  
552 model domain. This deflection does not occur symmetrically on both sides of each rift segment.  
553 Rather, it shows two distinct zones: 1) E-W orientations outside the rift deflect into a parallel  
554 orientation near the rift boarder or 2) N-S orientations outside of the rift deflect into E-W  
555 orientations near faults (Fig. 8j).

556

557 We find that  $S_{Hmax}$  orientations deflect gradually from E-W to N-S along abandoned rift  
558 boundary faults where activity ceased (Fig. 8h-j; upper left and lower right model domain). In

559 contrast,  $S_{Hmax}$  re-orientations from N-S to nearly E-W towards active rift boundary faults are  
560 followed by a rapid flip back to N-S along the faults (Fig. 8h-j; lower left and upper right model  
561 domain). The two types of re-orientation seem to correspond with two types of deformed  
562 zones. Where deformation is strongly localized along rift boundary faults, jumps in the  $S_{Hmax}$   
563 orientation occur. In contrast, zones where inward migration of fault activity activates intra-  
564 rift faults,  $S_{Hmax}$  re-orientation occurs gradually.

565

### 566 **3.7.3. Rift arm competition and deflection (y-seed models)**

567 A prominent feature in our models with two competing rift segments is the deflection of rift  
568 branches and arcuate strain rate patterns (Fig. 8a-e) in the model with a v-seed configuration.  
569 Moreover, the i-seed configuration demonstrates a gradual  $S_{Hmax}$  re-orientation over a broader  
570 pre-weakened zone due to formerly active boundary faults. One could therefore expect that  
571 both features should occur in the model with y-seed configuration (Fig. 8k-o).

572

573 Indeed, early stages (i.e., after 0.4 million years; Fig. 8k) are characterized by a symmetric  
574 stress field with re-oriented  $S_{Hmax}$  values near the two rear rift segments. However, in contrast  
575 to the v-seed configuration,  $S_{Hmax}$  re-orientation also occurs near the frontal pre-existing weak  
576 fabric along developing rift boundary faults. In the isotropic zone,  $S_{Hmax}$  values dominantly  
577 show a N-S direction. The general N-S orientation reflects the regional stress field due to an  
578 E-W extension as predicted by Anderson (1905) in isotropic areas, into which rift segments  
579 have yet to propagate. With ongoing extension, all three rift segments propagate into the  
580 isotropic zone and cause a re-orientation of  $S_{Hmax}$  (Fig. 8l). Note that after 0.8 million years  
581 the stress re-orientation occurs symmetrically. This contrasts with the i-seed configuration  
582 where  $S_{Hmax}$  values deflect into either an E-W orientation along active rift boundary faults or  
583 gradually turn into a fault parallel direction over a broader weakened zone (see subsection  
584 3.7.2.). The early symmetric stress distribution in the y-seed configuration model is

585 unarguably due to the symmetric seed configuration (see also Fig. 8a-e). At this stage, dip-  
586 slip faulting along the competing sub-parallel rift segments is favored over oblique slip faults  
587 as in models with a v-seed configuration. It is only after 1.2 million years, when fault activity  
588 along the right rear segment ceases that deformation localizes along the left rear and frontal  
589 segments and linkage intensifies (Fig. 8m). Successively, localization and linkage occur  
590 coevally with a switch from a symmetric to an asymmetric stress distribution and resembles  
591 more the stress distribution in the i-seed configuration model (Fig. 8f-j). The model state after  
592 1.2 million years (Fig. 8m) also marks the switch from a symmetric to an asymmetric stress  
593 distribution that was formerly dominated by the competing rear rift segments with dip-slip  
594 faulting favored along the two competing rift segments (see also v-seed configuration; Fig. 8  
595 a-e). After 1.2 million years the system is dominated by the linkage of two obliquely oriented  
596 segments (i.e., i-seed configuration). Note that after 1.2 million years dip-slip faulting mostly  
597 occurs along the competing rift segment that links with the opposingly propagating segment  
598 whereas dominantly oblique slip faults occur along the abandoned rift segment where activity  
599 ceases.

600

601 The symmetry switch is also visible in rose diagrams of stress orientations within the active  
602 faulting zone (i.e., strain rate  $\geq 10^{-16} \text{ s}^{-1}$ ). A dominantly N-S oriented  $S_{Hmax}$  distribution changes  
603 to a bimodal distribution with a second E-W orientation (Fig. 8l-n). Similarly, bimodal  $S_{Hmax}$   
604 distribution is also visible in the experiment with an i-seed configuration but occurs earlier.  
605 Since the experiment with an i-seed configuration is never in the state of an early symmetric  
606 stress distribution linkage is facilitated and occurs earlier (Fig.8g-i).

607

#### 608 **4. Discussion**

609 Despite the relatively simple setup of our experiments, the interaction of individual weak seeds  
610 generates a complex evolution of linkage patterns. In the following we discuss the effect of

611 pre-existing structures on  $S_{Hmax}$  re-orientations and how, in return, stress re-orientation  
612 influences rift propagation and rift segment linkage.

613

614 **4.1. Effect of pre-existing structures on rift segment propagation,**  
615 **interaction, and  $S_{Hmax}$**

616 Previous modelling studies demonstrated that pre-existing weaknesses may cause local re-  
617 orientations of  $S_{Hmax}$  resulting in extensional faults with an oblique orientation to the regional  
618 extension direction which exhibit pure dip-slip behavior (e.g., Morley, 2010; Corti et al., 2013;  
619 Morley, 2017; Philippon et al., 2015). This contrasts the expected (assuming Andersonian  
620 faulting theory) occurrence of faults with an oblique slip component above pre-existing  
621 structures that are obliquely oriented with respect to the extension direction (Tron and Brun,  
622 1991; Withjack and Jamison, 1986). Our  $S_{Hmax}$  analysis documents two types of stress re-  
623 orientation, either gradually or by a jump along faults (Fig. 8i). A potential explanation for the  
624 two types of stress deflection is that cessation of boundary fault activity (and subsequent  
625 faulting activity along intra-rift faults) creates a broad zone of reduced crustal strength. Hence,  
626  $S_{Hmax}$  orientations successively re-orient along those formerly active faults and eventually  
627 rotate into a N-S orientation along active intra-rift faults. In contrast, where faulting activity  
628 is strongly localized along rift boundary faults, re-orientation occurs rapidly by a jump from E-  
629 W to a N-S orientation. This suggests that formerly active faults act as a wider zone of pre-  
630 weakened material, where stresses deflect sequentially rather than with a rapid jump. Similar  
631 observations have been made in previous studies of numerical models (Gudmundsson et al.,  
632 2010; Kattenhorn et al., 2000). These experiments suggest that earlier fractures lead to  
633 subzones (within a broader damage zone), where stresses subsequently rotate away from the  
634 regional stress field. Although our analog and numerical models do not feature elastic  
635 deformation, they indicate that stress deflection is an ongoing process, even after elastic  
636 material failure. Such a stress deflection further implies that stress orientations in rocks with

637 pre-existing weaknesses can substantially deviate from predicted orientations in isotropic  
638 media (Anderson, 1905).

639

640 It has been proposed that early faulting and propagation in the Rukwa and North Malawi Rifts  
641 (Fig. 1c) were guided by pre-existing basement fabrics (Heilman et al., 2019). This region is  
642 further shaped by a flip in the boundary fault polarity in the present-day geometry within the  
643 interaction zone between Rukwa Rift and North Malawi Rift (Bosworth, 1985). Our i-seed  
644 models show identical geometries for increasing intermediate angles (Figs. 7h,i and S5), where  
645 plastic strain near pre-existing structures is mostly accommodated along prominent rift  
646 boundary faults that flip fault polarity from the frontal to the rear rift segment. This flip in  
647 fault polarity occurs prominently in models with an intermediate angle  $\geq 10^\circ$ . We speculate  
648 that the increasing obliquity of the southward propagating rift segment favors asymmetric  
649 graben evolution with one dominant boundary fault accommodating a larger amount of strain.  
650 In contrast to small intermediate angles (i.e.,  $10^\circ$ ), seed configurations with a higher obliquity  
651 provoke local rotation of  $S_{Hmax}$  within the interaction zone into a strike-slip regime near the  
652 subordinate boundary fault (Fig. S5). Hence, strain accommodation along incipient faults  
653 within the dip-slip regime is favored. This facilitates propagation along those dominant rift  
654 boundary faults and eventually defines the final rift geometry.

655

656 Kolawole et al. (2018) further propose two different types of strain accommodation at early  
657 rift phases. Prominent strain accommodation localized onto a discrete and narrow zone along  
658 large rift boundary faults (Style-1; sensu Kolawole et al., 2018) and faulting distributed over  
659 a broader zone, where fault clusters may reflect pre-conditioning of the material (Style-2;  
660 sensu Kolawole et al., 2018). With this perspective, jumps and gradual rotation of  $S_{Hmax}$   
661 orientations are comparable to Style-1 and Style-2 strain localization, respectively, as  
662 proposed by Kolawole et al. (2018). Hence, the type of weakness (narrow discrete zone or

663 distributed cluster zone) should also be reflected by the stress re-orientation distribution  
664 (Morley, 2010).

665

#### 666 **4.2. Local $S_{Hmax}$ re-orientation and its influence on rift segment interaction** 667 **and rift deflection**

668 A particular observation in our experiments with a v-, and y-seed configuration is that two  
669 sub-parallel rift segments, which propagate approximately in the same direction deflect away  
670 from each other at early stages. This is somewhat surprising as one would expect the two rift  
671 segments to cut towards each other by minimizing fault length. The occurrence of rift  
672 deflection in both analog and numerical experiments validates that the results are robust and  
673 require discussing the role of  $S_{Hmax}$  re-orientation and how it influences rift segment  
674 interaction.

675

676 We speculate that, while both rear rift segments in our y-seed models equivalently  
677 accommodate strain in the early stages (i.e., when the overall stress distribution is symmetric;  
678 Fig. 8),  $S_{Hmax}$  orientations are dominated by the influence of the two competing rear rift  
679 segments that accommodate strain in equal parts. It is only after fault activity along one rear  
680 segment ceases that deformation localizes along the active rear and frontal segments and  
681 linkage intensifies. Strain localization and linkage occur coevally with a switch from a  
682 symmetric to an asymmetric stress distribution resembling the stress distributions in v-, and  
683 i-seed configuration models, respectively. The switch from a symmetric to an asymmetric  
684 stress distribution in y-seed models also marks the switch from a system that was formerly  
685 dominated by the competing rear rift segments (i.e., v-seed configuration) to a system that  
686 is dominated by the linkage of two obliquely oriented segments (i.e., i-seed configuration).

687



688 In models with a v-seed configuration, however, the symmetric phase prevails and causes  
689 coeval  $S_{Hmax}$  re-orientations and rift deflection that cause divergence of the two propagating  
690 rift segments. A similar process of extensional segment interaction via stress rotation is known  
691 from mid-ocean ridge settings: Pollard and Aydin (1984) argue that paths of two opposingly  
692 propagating oceanic ridges weakly diverge due to shear stresses that divert propagating ridges  
693 as they approach each other. Once the two ridges overlap, the stress field changes causing  
694 convergence and intersection. Similarly, Nelson et al. (1992) describe interference of  
695 compressional zones of propagating cracks diverting their tips before they overlap and turn  
696 back toward another. In this respect, our models with a v-seed configuration suggest that  
697 stresses also cause divergence of two rift segments that propagate approximately in the same  
698 direction. However, overlap never occurs (as they propagate approximately in the same  
699 direction) and hence, the two segments remain in a stress field that further diverts their paths.

700

701 Only in models with a y-seed configuration, compressional zones and rift deflection can be  
702 overcome once the opposingly propagating rift segment links with one of the competing rift  
703 segments. Linkage occurs after about the first million years, concurrently with rift deflection  
704 and abandonment of the right rear segment (Figs. 9a and S6). Moreover, remaining activity  
705 in the right rear segment depicts low strain rates along numerous arcuate intra-rift faults (Figs.  
706 9b and S6). This suggests that linkage and rift abandonment are closely coupled and faulting  
707 along the linked segments intensifies when the activity along the remaining rift segment  
708 ceases. In addition, the left rear segment displays a rather asymmetric half graben geometry  
709 (Figs. 5c,d, 7i and S4) with one prominent rift boundary fault accommodating a larger part of  
710 plastic strain similar to our models with a i-seed configuration (see also Figs. 7e,f and S5).  
711 Dominant strain accommodation occurs along the west-dipping rift boundary fault of the left  
712 rear segment coinciding with jumps in the  $S_{Hmax}$  orientation (Fig. 8m-o). Our modelling results  
713 show that stress deflection along rift segment tips is a mechanical consequence of the

714 interaction between weak zones and far-field stresses offering a potential explanation for  
715 naturally occurring rift deflection. However, we must emphasize that complexities in natural  
716 rift settings pose additional difficulties that require further investigations of stress orientations.

717

718 An example of rift deflection in nature has been described in the Main Ethiopian Rift.  
719 Geophysical and geologic studies evidence that pre-existing structures controlled the  
720 approximately 11 Ma southward propagation of the Northern Main Ethiopian Rift and its  
721 contemporaneous westward deflection along the Yerer-Tullu Wellel Volcanotectonic  
722 Lineament (YTVL; Abebe et al., 1998; Keranen and Klemperer, 2008; Muhabaw et al., 2022).  
723 Only after the rotation of the principal stress direction at about 5-6 Ma (Bonini et al., 2005),  
724 extension along the YTVL ceased and deformation localization along the Central Main  
725 Ethiopian Rift became more favorable. Our models document similar rift deflections and  
726 moreover indicate that, even in the absence of changing plate motions, rift segments deflect,  
727 and may cease while competing rift segments prevail and strain further localizes.

728

729 For the Canyonlands National Park, it has been proposed that it is mainly the lateral offset  
730 between pre-existing structures that explains the diversity of structures (Allken et al., 2013;  
731 Fig. 1d). With larger offsets, interaction between adjacent rift segments is limited and  
732 competing grabens persist and endure ongoing propagation coevally. We find that stresses,  
733 in combination with the geometry of pre-existing structures, play an important role and that  
734 they have a mutual effect on one another. Hence, stress distribution must be considered as  
735 an important factor especially in early rifting stages when segments link and predetermine  
736 strain localization during subsequent progressive rifting.

737

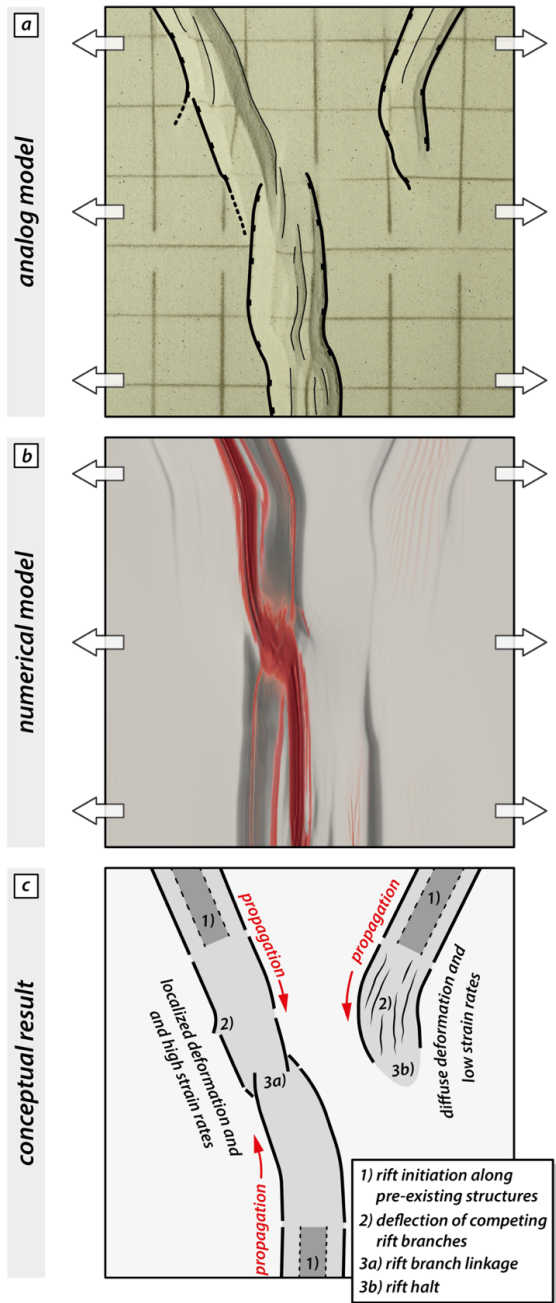


**Figure 9:** Summary plot showing the geometric similarity of rift segment linkage, deflection of competing branches and abandonment in analog and numerical models. a) Observed key features at the final stage of the analog model. b) Final strain and strain rate pattern in the numerical reference model. c) Conceptual interpretation of rift deflection and linkage based on our analog and numerical results (for details see text).

739 **5. Conclusions**

740 We present a series of analog and numerical rifting experiments. Our results suggest that,  
741 even in a relatively simple iso-viscous two-layer crustal setup, pre-existing weaknesses  
742 substantially disturb the regional stress pattern, which impacts rift propagation and the overall  
743 rift evolution. The complex stress re-orientation is distinct for different seed configurations  
744 (i.e., v-seed, i-seed, and y-seed) and closely interacts with the final rift geometry. The most  
745 important findings of our study can be summarized as follows:

746

- 747 • Our numerical experiments reproduce rift segment deflection seen in our analog  
748 models. This highlights the robustness of our results and their applicability to  
749 interpreting rift segment propagation, interaction, and linkage in natural settings of  
750 continental rifting.
- 751 • Pre-existing structures may control localization of rift segments that successively  
752 propagate into previously undeformed areas. Consequently, stress re-orientation  
753 initially occurs along pre-conditioned zones and propagates, coevally with rift segment  
754 propagation and strain accrual, into formerly undeformed areas.
- 755 • Interacting stresses between two competing rift segments may cause outward  
756 deflection of the propagating rift tips resulting in a successively broader rift geometry  
757 along-strike.
- 758 • Outward deflection of competing rift segments is less prominent if an opposingly  
759 propagating rift segment is present. With progressive extensional deformation, strain  
760 accrual along one of the competing rift segments prevails whilst faulting activity along  
761 the other segment ceases. Coevally, the general stress orientation changes from a  
762 symmetric to an asymmetric distribution indicating the onset of rift linkage.
- 763 • Our modelling results reproduce first-order structures of natural examples from the  
764 East African Rift System and, on smaller scale, graben structures in the Canyonlands

765 National Park. The combined investigation of surface stresses and strain localization  
766 provides an explanation for distinct rift deflection among competing rift segments and  
767 rift linkage structures where ongoing deformation and stresses mutually affect each  
768 other.

769

770 While changes in rift orientation are often used to infer [changes in plate-motion](#), we  
771 demonstrate that local stress field re-orientations can occur under constant plate motions.  
772 Albeit on a smaller scale, implications from our observations corroborate findings from  
773 previous studies (Brune; 2014; Duclaux et al., 2020; Gapais et al., 2000). Locally, stress and  
774 strain can largely deviate from a regional, far-field pattern and instead represent local  
775 deformation interference. In addition, the observed stress re-orientations change over time  
776 indicating that stresses measured in natural examples may depict transient stages that change  
777 with progressive deformation due to subsequent changes in material strengths (Morley et al.,  
778 2004). This implication must be considered in processing local fault-slip data when interpreting  
779 the evolution of rifts at any scale.

780

### 781 **Data availability**

782 Rheological measurements of the used analog materials are available in the form of open  
783 access data publications provided by the GFZ Data Service (brittle materials: Schmid et al.,  
784 2020a; Schmid et al., 2020b; viscous materials: Zwaan et al., 2018). [The input files and post  
785 processing scripts for reproducing the data have been deposited in the Zenodo repository:  
786 <https://zenodo.org/badge/latestdoi/610197324>.](#)

787

788

789

790

Deleted: regional palaeo-movements

792 **Acknowledgements**

793 We thank Esther Heckenbach for helpful assistance with post processing and visualization.  
794 The work was supported by the North-German Supercomputing Alliance (HLRN). We thank  
795 the Swiss National Science Foundation for providing financial support. Finally, we thank the  
796 two [Referees](#), Guillaume Duclaux and Chris Morley [as well as Topical Editor Patrice Rey](#) for  
797 their detailed, constructive and motivating comments that significantly helped to improve this  
798 manuscript.

Deleted: reviewers

799

800 **Funding**

801 This project is supported by the Swiss National Science Foundation [grant number  
802 200021\_178731].

803

804 **CRedit authorship contribution statement**

805 Timothy C. Schmid: Conceptualization, Methodology, Investigation, Formal Analysis, Writing  
806 – original draft, Visualization, Data curation. Sascha Brune: Conceptualization, Methodology,  
807 HPC funding acquisition, Supervision, Project administration, Writing – review & editing. Anne  
808 Glerum: Methodology, Software, HPC funding acquisition, Writing – review & editing. Guido  
809 Schreurs: Writing – review & editing, Supervision, Project administration, Funding acquisitions,  
810 Resources.

811

813 **References**

- 814 Abebe, T., Mazzarini, F., Innocenti, F., and Manetti, P.: The Yerer-Tullu Wellel volcanotectonic lineament: A  
815 transtensional structure in central Ethiopia and the associated magmatic activity, *Journal of African Earth Sciences*,  
816 26, 135-150, 1998.  
817 [https://doi.org/10.1016/S0899-5362\(97\)00141-3](https://doi.org/10.1016/S0899-5362(97)00141-3)  
818  
819 Acocella, V., Faccenna, C., Funicello, R., and Rossetti, F.: Sand-box modelling of basement-controlled transfer  
820 zones in extensional domains, *Terra Nova-Oxford*, 11, 149-156, 1999.  
821  
822 Adam, J., Urai, J., Wieneke, B., Oncken, O., Pfeiffer, K., Kukowski, N., Lohrmann, J., Hoth, S., Van Der Zee, W.,  
823 and Schmatz, J.: Shear localisation and strain distribution during tectonic faulting—New insights from granular-  
824 flow experiments and high-resolution optical image correlation techniques, *Journal of Structural Geology*, 27, 283-  
825 301, 2005.  
826 <https://doi.org/10.1016/j.jsg.2004.08.008>  
827  
828 Allken, V., Huismans, R. S., and Thieulot, C.: Three-dimensional numerical modeling of upper crustal extensional  
829 systems, *Journal of Geophysical Research: Solid Earth*, 116, 2011.  
830 <https://doi.org/10.1029/2011JB008319>  
831  
832 Allken, V., Huismans, R. S., and Thieulot, C.: Factors controlling the mode of rift interaction in brittle-ductile coupled  
833 systems: A 3D numerical study, *Geochemistry, Geophysics, Geosystems*, 13, 2012.  
834 <https://doi.org/10.1029/2012GC004077>  
835  
836 Allken, V., Huismans, R. S., Fossen, H., and Thieulot, C.: 3D numerical modelling of graben interaction and linkage:  
837 a case study of the Canyonlands grabens, Utah, *Basin Research*, 25, 436-449, 2013.  
838 <https://doi.org/10.1111/bre.12010>  
839  
840 Anderson, E. M.: The dynamics of faulting, *Transactions of the Edinburgh Geological Society*, 8, 387-402, 1905.  
841 <https://doi.org/10.1144/transed.8.3.387>  
842  
843 Bellahsen, N. and Daniel, J. M.: Fault reactivation control on normal fault growth: an experimental study, *Journal*  
844 *of Structural Geology*, 27, 769-780, 2005.  
845 <https://doi.org/10.1016/j.jsg.2004.12.003>  
846  
847 Bonini, M., Corti, G., Innocenti, F., Manetti, P., Mazzarini, F., Abebe, T., and Pecsckay, Z.: Evolution of the Main  
848 Ethiopian Rift in the frame of Afar and Kenya rifts propagation, *Tectonics*, 24, 2005.  
849 <https://doi.org/10.1029/2004TC001680>  
850  
851 Bosworth, W.: Geometry of propagating continental rifts, *Nature*, 316, 625-627, 1985.  
852 <https://doi.org/10.1038/316625a0>  
853  
854 Brune, S.: Evolution of stress and fault patterns in oblique rift systems: 3-D numerical lithospheric-scale  
855 experiments from rift to breakup, *Geochemistry, Geophysics, Geosystems*, 15, 3392-3415, 2014.  
856 <https://doi.org/10.1002/2014GC005446>  
857  
858 Brune, S. and Autin, J.: The rift to break-up evolution of the Gulf of Aden: Insights from 3D numerical lithospheric-  
859 scale modelling, *Tectonophysics*, 607, 65-79, 10.1016/j.tecto.2013.06.029, 2013.  
860 <https://doi.org/10.1016/j.tecto.2013.06.029>  
861  
862 Brune, S., Corti, G., and Ranalli, G.: Controls of inherited lithospheric heterogeneity on rift linkage: Numerical and  
863 analog models of interaction between the Kenyan and Ethiopian rifts across the Turkana depression, *Tectonics*,  
864 36, 1767-1786, 2017.  
865 <https://doi.org/10.1002/2017TC004739>  
866  
867 Brune, S., Popov, A. A., and Sobolev, S. V.: Modeling suggests that oblique extension facilitates rifting and  
868 continental break-up, *Journal of Geophysical Research: Solid Earth*, 117, 2012.  
869 <https://doi.org/10.1029/2011JB008860>  
870  
871 Childs, C., Watterson, J., and Walsh, J.: Fault overlap zones within developing normal fault systems, *Journal of the*  
872 *Geological Society*, 152, 535-549, 1995.  
873 <https://doi.org/10.1144/gsjgs.152.3.0535>  
874

875 Collanega, L., Jackson, C. A.-L., Bell, R., Coleman, A. J., Lenhart, A., and Breda, A.: How do intra-basement fabrics  
876 influence normal fault growth? Insights from the Taranaki Basin, offshore New Zealand, 2018.  
877 <https://doi.org/10.31223/osf.io/8rn9u>  
878  
879 Corti, G.: Evolution and characteristics of continental rifting: Analog modeling-inspired view and comparison with  
880 examples from the East African Rift System, *Tectonophysics*, 522-523, 1-33, 10.1016/j.tecto.2011.06.010, 2012.  
881 <https://doi.org/10.1016/j.tecto.2011.06.010>  
882  
883 Corti, G., van Wijk, J., Cloetingh, S., and Morley, C. K.: Tectonic inheritance and continental rift architecture:  
884 Numerical and analogue models of the East African Rift system, *Tectonics*, 26, 2007.  
885 <https://doi.org/10.1029/2006TC002086>  
886  
887 Corti, G., Philippon, M., Sani, F., Keir, D., and Kidane, T.: Re-orientation of the extension direction and pure  
888 extensional faulting at oblique rift margins: Comparison between the Main Ethiopian Rift and laboratory  
889 experiments, *Terra Nova*, 25, 396-404, 2013.  
890 <https://doi.org/10.1111/ter.12049>  
891  
892 Corti, G., Cioni, R., Franceschini, Z., Sani, F., Scaillet, S., Molin, P., Isola, I., Mazzarini, F., Brune, S., and Keir, D.:  
893 Aborted propagation of the Ethiopian rift caused by linkage with the Kenyan rift, *Nature communications*, 10, 1-  
894 11, 2019.  
895 <https://doi.org/10.1038/s41467-019-09335-2>  
896  
897 Crameri, F., Shephard, G. E., and Heron, P. J.: The misuse of colour in science communication, *Nature*  
898 *communications*, 11, 1-10, 2020.  
899 <https://doi.org/10.1038/s41467-020-19160-7>  
900  
901 Daly, M., Chorowicz, J., and Fairhead, J.: Rift basin evolution in Africa: the influence of reactivated steep basement  
902 shear zones, Geological Society, London, Special Publications, 44, 309-334, 1989.  
903 <https://doi.org/10.1144/GSL.SP.1989.044.01.17>  
904  
905 Duclaux, G., Huismans, R. S., and May, D. A.: Rotation, narrowing, and preferential reactivation of brittle structures  
906 during oblique rifting, *Earth and Planetary Science Letters*, 531, 115952, 2020.  
907 <https://doi.org/10.1016/j.epsl.2019.115952>  
908  
909 Duffy, O. B., Bell, R. E., Jackson, C. A.-L., Gawthorpe, R. L., and Whipp, P. S.: Fault growth and interactions in a  
910 multiphase rift fault network: Horda Platform, Norwegian North Sea, *Journal of Structural Geology*, 80, 99-119,  
911 2015.  
912 <https://doi.org/10.1016/j.jsg.2015.08.015>  
913  
914 Duretz, T., de Borst, R., and Le Pourhiet, L.: Finite thickness of shear bands in frictional viscoplasticity and  
915 implications for lithosphere dynamics, *Geophysics, Geosystems*, 20, 5598-5616, 2019.  
916 <https://doi.org/10.1029/2019GC008531>  
917  
918 Ebinger, C., Yemane, T., Harding, D., Tesfaye, S., Kelley, S., and Rex, D.: Rift deflection, migration, and  
919 propagation: Linkage of the Ethiopian and Eastern rifts, Africa, *Geological Society of America Bulletin*, 112, 163-  
920 176, 2000.  
921 [https://doi.org/10.1130/0016-7606\(2000\)112<163:RDMAPL>2.0.CO;2](https://doi.org/10.1130/0016-7606(2000)112<163:RDMAPL>2.0.CO;2)  
922  
923 Gapais, D., Cobbold, P. R., Bourgeois, O., Rouby, D., and de Urreiztieta, M.: Tectonic significance of fault-slip data,  
924 *Journal of Structural Geology*, 22, 881-888, 2000.  
925 [https://doi.org/10.1016/S0191-8141\(00\)00015-8](https://doi.org/10.1016/S0191-8141(00)00015-8)  
926  
927 Gassmüller, R., Lokavarapu, H., Heien, E., Puckett, E. G., and Bangerth, W.: Flexible and scalable particle-in-cell  
928 methods with adaptive mesh refinement for geodynamic computations, *Geochemistry, Geophysics, Geosystems*,  
929 19, 3596-3604, 2018.  
930 <https://doi.org/10.1029/2018GC007508>  
931  
932 Glerum, A., Brune, S., Stamps, D. S., and Strecker, M. R.: Victoria continental microplate dynamics controlled by  
933 the lithospheric strength distribution of the East African Rift, *Nature Communications*, 11, 1-15, 2020.  
934 <https://doi.org/10.1038/s41467-020-16176-x>  
935  
936 Glerum, A., Thieulot, C., Fraters, M., Blom, C., and Spakman, W.: Nonlinear viscoplasticity in ASPECT:  
937 benchmarking and applications to subduction, *Solid Earth*, 9, 267-294, 2018.  
938 <https://doi.org/10.5194/se-9-267-2018>



939 Gudmundsson, A., Simmenes, T. H., Larsen, B., and Philipp, S. L.: Effects of internal structure and local stresses  
940 on fracture propagation, deflection, and arrest in fault zones, *Journal of Structural Geology*, 32, 1643-1655, 2010.  
941 <https://doi.org/10.1016/j.jsg.2009.08.013>  
942  
943 Heidbach, O., Rajabi, M., Cui, X., Fuchs, K., Müller, B., Reinecker, J., Reiter, K., Tingay, M., Wenzel, F., and Xie,  
944 F.: The World Stress Map database release 2016: Crustal stress pattern across scales, *Tectonophysics*, 744, 484-  
945 498, 2018.  
946 <https://doi.org/10.1016/j.tecto.2018.07.007>  
947  
948 Heilman, E., Kolawole, F., Atekwana, E. A., and Mayle, M.: Controls of Basement Fabric on the Linkage of Rift  
949 Segments, *Tectonics*, 38, 1337-1366, 10.1029/2018tc005362, 2019.  
950 <https://doi.org/10.1029/2018TC005362>  
951  
952 Heister, T., Dannberg, J., Gassmüller, R., and Bangerth, W.: High accuracy mantle convection simulation through  
953 modern numerical methods–II: realistic models and problems, *Geophysical Journal International*, 210, 833-851,  
954 2017.  
955 <https://doi.org/10.1029/2018TC005362>  
956  
957 Jacquey, A. B. and Cacace, M.: Multiphysics modeling of a brittle-ductile lithosphere: 2. Semi-brittle, semi-ductile  
958 deformation and damage rheology, *Journal of Geophysical Research: Solid Earth*, 125, e2019JB018475, 2020.  
959 <https://doi.org/10.1029/2019JB018475>  
960  
961 Kattenhorn, S. A., Aydin, A., and Pollard, D. D.: Joints at high angles to normal fault strike: an explanation using  
962 3-D numerical models of fault-perturbed stress fields, *Journal of structural Geology*, 22, 1-23, 2000.  
963 [https://doi.org/10.1016/S0191-8141\(99\)00130-3](https://doi.org/10.1016/S0191-8141(99)00130-3)  
964  
965 Katzman, R., ten Brink, U. S., and Lin, J.: Three-dimensional modeling of pull-apart basins: Implications for the  
966 tectonics of the Dead Sea Basin, *Journal of Geophysical Research: Solid Earth*, 100, 6295-6312, 1995.  
967 <https://doi.org/10.1029/94JB03101>  
968  
969 Keranen, K. and Klemperer, S.: Discontinuous and diachronous evolution of the Main Ethiopian Rift: Implications  
970 for development of continental rifts, *Earth and Planetary Science Letters*, 265, 96-111, 2008.  
971 <https://doi.org/10.1016/j.epsl.2007.09.038>  
972  
973 Koehn, D., Aanyu, K., Haines, S., and Sachau, T.: Rift nucleation, rift propagation and the creation of basement  
974 micro-plates within active rifts, *Tectonophysics*, 458, 105-116, 2008.  
975 <https://doi.org/10.1016/j.tecto.2007.10.003>  
976  
977 Kolawole, F., Phillips, T. B., Atekwana, E. A., and Jackson, C. A.-L.: Structural inheritance controls strain distribution  
978 during early continental rifting, rukwa rift, *Frontiers in Earth Science*, 670, 2021.  
979 <https://doi.org/10.3389/feart.2021.707869>  
980  
981 Kolawole, F., Atekwana, E. A., Laó-Dávila, D. A., Abdelsalam, M. G., Chindandali, P. R., Salima, J., and Kalindekafe,  
982 L.: Active Deformation of Malawi Rift's North Basin Hinge Zone Modulated by Reactivation of Preexisting  
983 Precambrian Shear Zone Fabric, *Tectonics*, 37, 683-704, 10.1002/2017tc004628, 2018.  
984 <https://doi.org/10.1002/2017TC004628>  
985  
986 Kronbichler, M., Heister, T., and Bangerth, W.: High accuracy mantle convection simulation through modern  
987 numerical methods, *Geophysical Journal International*, 191, 12-29, 2012.  
988 <https://doi.org/10.1111/j.1365-246X.2012.05609.x>  
989  
990 Lavier, L. L., Buck, W. R., and Poliakov, A. N.: Factors controlling normal fault offset in an ideal brittle layer, *Journal*  
991 *of Geophysical Research: Solid Earth*, 105, 23431-23442, 2000.  
992 <https://doi.org/10.1029/2000JB900108>  
993  
994 Macdonald, K. C. and Fox, P.: Overlapping spreading centres: New accretion geometry on the East Pacific Rise,  
995 *Nature*, 302, 55-58, 1983.  
996 <https://doi.org/10.1038/302055a0>  
997  
998 Mills, N.: Dislocation array elements for the analysis of crack and yielded zone growth, *Journal of Materials Science*,  
999 16, 1317-1331, 1981.  
1000 <https://doi.org/10.1007/BF01033848>  
1001

1002 Mondy, L. S., Rey, P. F., Duclaux, G., and Moresi, L.: The role of asthenospheric flow during rift propagation and  
1003 breakup, *Geology*, 46, 103-106, 2018.  
1004 <https://doi.org/10.1130/G39674.1>  
1005  
1006 Morley, C.: Stress re-orientation along zones of weak fabrics in rifts: An explanation for pure extension in 'oblique'  
1007 rift segments?, *Earth and Planetary Science Letters*, 297, 667-673, 2010.  
1008 <https://doi.org/10.1016/j.epsl.2010.07.022>  
1009  
1010 Morley, C.: The impact of multiple extension events, stress rotation and inherited fabrics on normal fault geometries  
1011 and evolution in the Cenozoic rift basins of Thailand, *Geological Society, London, Special Publications*, 439, 413-  
1012 445, 2017.  
1013 <https://doi.org/10.1144/SP439.3>  
1014  
1015 Morley, C., Nelson, R., Patton, T., and Munn, S.: Transfer zones in the East African rift system and their relevance  
1016 to hydrocarbon exploration in rifts, *AAPG bulletin*, 74, 1234-1253, 1990.  
1017 <https://doi.org/10.1306/0C9B2475-1710-11D7-8645000102C1865D>  
1018  
1019 Morley, C., Haranya, C., Phoosongsee, W., Pongwapee, S., Kornsawan, A., and Wonganan, N.: Activation of rift  
1020 oblique and rift parallel pre-existing fabrics during extension and their effect on deformation style: examples from  
1021 the rifts of Thailand, *Journal of Structural Geology*, 26, 1803-1829, 2004.  
1022 <https://doi.org/10.1016/j.jsg.2004.02.014>  
1023  
1024 Morley, C. K.: Patterns of displacement along large normal faults: implications for basin evolution and fault  
1025 propagation, based on examples from East Africa, *AAPG bulletin*, 83, 613-634, 1999.  
1026 <https://doi.org/10.1306/00AA9C0A-1730-11D7-8645000102C1865D>  
1027  
1028 Muhabaw, Y., Muluneh, A. A., Nugsse, K., Gebru, E. F., and Kidane, T.: Paleomagnetism of Gedemsa magmatic  
1029 segment, Main Ethiopian Rift: Implication for clockwise rotation of the segment in the Early Pleistocene,  
1030 *Tectonophysics*, 838, 229475, 2022.  
1031 <https://doi.org/10.1016/j.tecto.2022.229475>  
1032  
1033 Nelson, R., Patton, T., and Morley, C.: Rift-segment interaction and its relation to hydrocarbon exploration in  
1034 continental rift systems, *AAPG bulletin*, 76, 1153-1169, 1992.  
1035 <https://doi.org/10.1306/BDF898E-1718-11D7-8645000102C1865D>  
1036  
1037 Oliva, S. J., Ebinger, C. J., Rivalta, E., Williams, C. A., Wauthier, C., and Currie, C. A.: State of stress and stress  
1038 rotations: Quantifying the role of surface topography and subsurface density contrasts in magmatic rift zones  
1039 (Eastern Rift, Africa), *Earth and Planetary Science Letters*, 584, 117478, 2022.  
1040 <https://doi.org/10.1016/j.epsl.2022.117478>  
1041  
1042 Philippon, M., Willingshofer, E., Sokoutis, D., Corti, G., Sani, F., Bonini, M., and Cloetingh, S.: Slip re-orientation in  
1043 oblique rifts, *Geology*, 43, 147-150, 2015.  
1044 <https://doi.org/10.1130/G36208.1>  
1045  
1046 Pollard, D. D. and Aydin, A.: Propagation and linkage of oceanic ridge segments, *Journal of Geophysical Research:*  
1047 *Solid Earth*, 89, 10017-10028, 1984.  
1048 <https://doi.org/10.1029/JB089iB12p10017>  
1049  
1050 Rose, I., Buffett, B., and Heister, T.: Stability and accuracy of free surface time integration in viscous flows, *Physics*  
1051 *of the Earth and Planetary Interiors*, 262, 90-100, 2017.  
1052 <https://doi.org/10.1016/j.pepi.2016.11.007>  
1053  
1054 Rosendahl, B. R.: Architecture of continental rifts with special reference to East Africa, *Annual Review of Earth and*  
1055 *Planetary Sciences*, 15, 445, 1987.  
1056 <https://doi.org/10.1146/annurev.ea.15.050187.002305>  
1057  
1058 Saria, E., Calais, E., Stamps, D., Delvaux, D., and Hartnady, C.: Present-day kinematics of the East African Rift,  
1059 *Journal of Geophysical Research: Solid Earth*, 119, 3584-3600, 2014.  
1060 <https://doi.org/10.1002/2013JB010901>  
1061  
1062 Schmid, T., Schreurs, G., Warsitzka, M., and Rosenau, M.: Effect of sieving height on density and friction of brittle  
1063 analogue material: ring-shear test data of quartz sand used for analogue experiments in the Tectonic Modelling Lab  
1064 of the University of Bern, 2020a.  
1065 <https://doi.org/10.5880/fidgeo.2020.006>

1066 Schmid, T., Schreurs, G., Warsitzka, M., and Rosenau, M.: Effect of sieving height on density and friction of brittle  
1067 analogue material: Ring-shear test data of corundum sand used for analogue experiments in the Tectonic Modelling  
1068 Lab of the University of Bern (CH), 2020b.  
1069 <https://doi.org/10.5880/fidgeo.2020.005>  
1070  
1071 Schultz-Ela, D. and Walsh, P.: Modeling of grabens extending above evaporites in Canyonlands National Park, Utah,  
1072 Journal of Structural Geology, 24, 247-275, 2002.  
1073 [https://doi.org/10.1016/S0191-8141\(01\)00066-9](https://doi.org/10.1016/S0191-8141(01)00066-9)  
1074  
1075 Tingay, M., Muller, B., Reinecker, J., and Heidbach, O.: State and origin of the present-day stress field in  
1076 sedimentary basins: New results from the World Stress Map Project, Golden Rocks 2006, The 41st US Symposium  
1077 on Rock Mechanics (USRMS).  
1078  
1079 Tingay, M. R., Morley, C. K., Hillis, R. R., and Meyer, J.: Present-day stress orientation in Thailand's basins, Journal  
1080 of Structural Geology, 32, 235-248, 2010.  
1081 <https://doi.org/10.1016/j.jsg.2009.11.008>  
1082  
1083 Tron, V. and Brun, J.-P.: Experiments on oblique rifting in brittle-ductile systems, Tectonophysics, 188, 71-84,  
1084 1991.  
1085 [https://doi.org/10.1016/0040-1951\(91\)90315-J](https://doi.org/10.1016/0040-1951(91)90315-J)  
1086  
1087 Trudgill, B. D.: Structural controls on drainage development in the Canyonlands grabens of southeast Utah, AAPG  
1088 bulletin, 86, 1095-1112, 2002.  
1089 <https://doi.org/10.1306/61EEDC2E-173E-11D7-8645000102C1865D>  
1090  
1091 Willemse, E. J.: Segmented normal faults: Correspondence between three-dimensional mechanical models and  
1092 field data, Journal of Geophysical Research: Solid Earth, 102, 675-692, 1997.  
1093 <https://doi.org/10.1029/96JB01651>  
1094  
1095 Willemse, E. J., Pollard, D. D., and Aydin, A.: Three-dimensional analyses of slip distributions on normal fault arrays  
1096 with consequences for fault scaling, Journal of Structural Geology, 18, 295-309, 1996.  
1097 [https://doi.org/10.1016/S0191-8141\(96\)80051-4](https://doi.org/10.1016/S0191-8141(96)80051-4)  
1098  
1099 Withjack, M. O. and Jamison, W. R.: Deformation produced by oblique rifting, Tectonophysics, 126, 99-124, 1986.  
1100 [https://doi.org/10.1016/0040-1951\(86\)90222-2](https://doi.org/10.1016/0040-1951(86)90222-2)  
1101  
1102 Zoback, M. L.: First-and second-order patterns of stress in the lithosphere: The World Stress Map Project, Journal  
1103 of Geophysical Research: Solid Earth, 97, 11703-11728, 1992.  
1104 <https://doi.org/10.1029/92JB00132>  
1105  
1106 Zwaan, F. and Schreurs, G.: How oblique extension and structural inheritance influence rift segment interaction:  
1107 Insights from 4D analog models, Interpretation, 5, SD119-SD138, 2017.  
1108 <https://doi.org/10.1190/INT-2016-0063.1>  
1109  
1110 Zwaan, F., Schreurs, G., Naliboff, J., and Buitter, S. J. H.: Insights into the effects of oblique extension on continental  
1111 rift interaction from 3D analogue and numerical models, Tectonophysics, 693, 239-260,  
1112 10.1016/j.tecto.2016.02.036, 2016.  
1113 <https://doi.org/10.1016/j.tecto.2016.02.036>  
1114  
1115 Zwaan, F., Schreurs, G., Ritter, M., Santimano, T., and Rosenau, M.: Rheology of PDMS-corundum sand mixtures  
1116 from the Tectonic Modelling Lab of the University of Bern (CH), 2018.  
1117 <http://doi.org/10.5880/fidgeo.2018.023>  
1118  
1119